An ALMA search for substructure and fragmentation in starless cores in Orion B North

by

Samuel Dumaresq Fielder
B.Sc., University of Alberta, 2018

A Thesis Submitted in Partial Fulfillment of the
Requirements for the Degree of

MASTER OF SCIENCE

in the Department of Physics and Astronomy

University of Victoria

An ALMA search for substructure and fragmentation in starless cores in Orion B North

by

Samuel Dumaresq Fielder
B.Sc., University of Alberta, 2018

Supervisory Committee

Dr. Helen Kirk, Co-Supervisor
(Department of Physics and Astronomy)

Dr. Kim Venn, Co-Supervisor
(Department of Physics and Astronomy)

Abstract

We present Atacama Large Millimeter/submillimeter Array (ALMA) Cycle 3 observations of 73 starless and protostellar cores in the Orion B North molecular cloud. We detect a total of 34 continuum sources at 106 GHz, and after comparisons with other data, 4 of these sources appear to be starless. Three of these starless core detections are found at the edges of target fields, while the final one detection matches the peak of a starless core. We use synthetic observations of starless core collapse under the turbulent fragmentation model, to compute the expected number of starless cores that should be detectable with our ALMA observations and find one starless core should be detectable, consistent with our data. Comparable ALMA analyses have now been performed on three nearby molecular clouds; the number of detections in Orion B North and Ophiuchus are consistent with the turbulent fragmentation predictions, while the lack of detections in Chamaeleon I is inconsistent. We perform a virial analysis of the starless core population in all three clouds to test whether or not core boundedness can explain the differences in the number of ALMA observations. Using a simple alpha parameter analysis, we find that the starless core population in Chamaeleon I is systematically more unbound compared to Ophiuchus and Orion B North. With the addition of external pressure binding terms in our analysis, we conclude that the Chamaeleon I dense core population is still less bounded than the other two clouds. Furthermore, the pressure binding in Chamaeleon I contributes typically an order of magnitude more to the overall core boundedness than the other two regions. These differences may explain why the Chamaeleon I cores do not follow the turbulent fragmentation model predictions, while the Ophiuchus and Orion B North cores are consistent with the model.

Table of Contents

List of Tables

List of Figures

Acknowledgements

Foremost, I wholeheartedly express my deepest thanks to my supervisor Dr. Helen Kirk for the ongoing and continuing support, and for her patience and immense knowledge base that have supported my study and research. I would also like to thank Dr. Karun Thanjavur for the vast amount of outreach opportunities that have kept an inherent balance in my otherwise engaged student lifestyle.

I would also like to give thanks to the following individuals that have contributed to this thesis work: Dr. Michael Dunham and Dr. Stella Offner for their contributions of the datasets and comments on initial results, Dr. James Di Francesco for his reassurance on my early interferometry imaging results, and Dr. John Tobin, my external examiner, for the fantastic feedback and recommendations on the entire work.

Lastly, and certainly not least, I would like to thank my partner, who has supported me in many more ways than one throughout my post secondary education, and especially so, over the last two years in Victoria. Without her, I would not be where I am today.

I acknowledge and respect the Lekwungen-speaking peoples on whose traditional territories I work and live, and the Songhees, Esquimalt and WSANEC peoples whose historical relationships with the land continue to this day.

I acknowledge and respect the separate cultures collectively known as the Atacameños or the Likan Antai, whose traditional territories most observatories in the Atacama Desert are located, including the site for the Atacama Large Millimeter/submillimeter Array.

Chapter 1

Introduction

Dense molecular cloud cores, sub-parsec scale (< 0.2 pc) over-densities within molecular clouds, are the immediate progenitors of stars (Bergin & Tafalla, 2007; di Francesco et al., 2007). Star formation is an inherently multi-scale process, and we access the wide variety of scales, from cloud to core, by way of different observations. The types of structures present at each scale may provide evidence as to which physical processes are dominant and how they govern star formation. Turbulence is thought to offer global support to the overall molecular cloud collapse, while also driving local collapse at the core scale (Mac Low & Klessen, 2004; Ballesteros-Paredes et al., 2007). Studies of the role of turbulence in the transition from dense cores to individual protostars can provide a deeper understanding for hallmark results in the theory of star formation, such as the initial mass function (Goodwin et al., 2008; Holman et al., 2013; Offner et al., 2014), and protostellar multiplicity (Chen et al., 2013; Lomax et al., 2015; Offner et al., 2022).

Around half of all solar-type stars exist in binary or multiple systems (Moe & Di Stefano, 2017), likely driven by some combination of disk fragmentation, core fragmentation and dynamical capture (see recent review by Offner et al., 2022). Recent observational studies in the Perseus cloud (Tobin et al., 2016) and the Orion cloud (Tobin et al., 2020) show that there is a distinct bimodal distribution in the separations of multiple stars systems, with peaks at ~ 75 AU and ~ 3000 AU. Tobin et al. (2020) attribute the larger separation peak to core fragmentation processes, while the smaller peak is attributed to disk fragmentation processes. Additionally, Kuruwita & Haugbølle (2023) used simulations of star formation in giant molecular clouds to show that a large population of smaller separation multiples could be attributed to significant orbital evolution of core fragmentation.

Large field-of-view (sub)millimeter observations have proven useful as a way of efficiently mapping entire star forming regions and their dense core populations. These dust continuum studies are good tracers of column density peaks, and can therefore characterize the locations, sizes and approximate masses of entire dense core populations (e.g., Motte et al., 1998; Enoch et al., 2007; Ward-Thompson et al., 2007; Könyves et al., 2015). Early (sub)millimetre studies indicated that starless cores have inner flat density substructures (Ward-Thompson et al., 1994), and that the density profiles are characterized by smooth Bonnor-Ebert (BE) spheres, which are centrally flat, and roughly drop as r^{-2} toward the edge (Ebert, 1955; Bonnor, 1956). These single-dish (sub)millimetre observations lack the sufficient angular resolution to probe the inner structures where fragmentation could be taking place.

High resolution facilities, like interferometers, are needed to be able to resolve the structure present within dense cores, leading to a more complete look at the role of core fragmentation. The earliest large interferometric survey of dense cores was a CARMA (Combined Array for Research in Millimetre-wave Astronomy) survey of 12 dense cores in the Perseus molecular cloud (Schnee et al., 2010). Despite observing each core for 8 hours, no detectable substructure was found (Schnee et al., 2010). Offner et al. (2012) showed that CARMA most likely lacked the sensitivity needed to detect substructure, and that the Atacama Large Millimetre/submillimetre Array (ALMA), will have the necessary sensitivity to see core substructure resulting from fragmentation.

Interferometers, by nature are only sensitive to a range of angular scales, the values of which are set by the observed wavelength and separations between antennas. Due to this nature, there is a maximum resolvable scale inherent to the observations taken, and in general diffuse structures are more difficult to observe than compact emission structures. If features, like those characterized by the inner flat density profiles of BE sphere-like cores, vary on scales larger than the maximum recoverable scale, those features may invisible in the data.

The first dense core population study conducted with ALMA was performed by Dunham et al. (2016) in the Chamealeon I region, where no detections were found for any of the 56 starless cores observed, whereas two such starless core detections were expected based on comparison with synthetic observations of simulations of turbulent starless core evolution. Dunham et al. (2016) also demonstrated that structures generated from turbulent fragmentation should be detected at a rate approximately 100 times higher than BE sphere modeled cores, for their specific ALMA observations. Thereafter, Kirk et al. (2017a) performed a population study of the L1688 molecular cloud in Ophiuchus, where the predictions derived from synthetic observations of the same turbulent fragmentation simulations matched the observed two compact substructure detections. Further studies by Tsitali et al. (2015) concluded that the dense core population in the Chamealeon I cloud appeared unbound, providing a possible explanation for the discrepancy between the turbulent model predictions and the observations.

Other survey-type observations have recently been taken in other nearby star forming regions, using different wavelength and antenna configurations, leading to a range of sensitivity in different spatial scales. Tokuda et al. (2020) performed survey-type observations with the ALMA Atacama Compact Array (ACA), of 39 dense cores (32 of which were starless) in the Taurus molecular cloud. Due to the observed wavelength chosen, Tokuda et al. (2020) achieved an angular resolution of $6.5''$ (~ 900AU) and detected complex substructures with a typical size scale of ~ 1000AU. These complex substructures, however, are typically very low signal to noise ($3-5$ times the local rms), and exhibit fairly small separations (a few times the beamsize). In this regime, the substructures may arise from noise in the interferometric data and are not reliably tracing multiple distinct features (Caselli et al., 2019; Tokuda et al., 2020). Tokuda et al. (2020) do succeed in detecting 20 out of the total 32 starless cores observed, yielding a success rate much higher than previously similar studies.

Additionally, Sahu et al. (2021), through the ALMA Survey of Orion Planck Galactic Cold Clumps (ALMASOP), have performed studies on the substructure probing much high resolution scales, down to $0.8''$ (~ 320AU) for a chosen starless core. The substructures show signatures of fragmentation, characterized by relatively high density ($2-8\times10^{7}$ cm^{-3}) and separations of $\sim$ 1200AU (Sahu et al., 2021). Both Tokuda et al. (2020) and Sahu et al. (2021) do not explicitly test the number of starless core expectations under a turbulent fragmentation model.

The current inconclusive tests of the turbulent fragmentation model highlights the need for further cloud-wide population studies. The Orion molecular cloud complex is a large, high mass star forming region, with the Orion B North portion situated approximately 419 pc away (Zucker et al., 2019). We utilize this change in environment and difference in dense core population, to add additional statistics revolving around the turbulent fragmentation model.

We present an ALMA 3mm continuum survey of 73 dense cores in the Orion B North molecular cloud. In Section 2, we present the observations and data reduction applied, and in Section 3, we perform a catalog search for any associated protostellar sources. In Section 4 we analyze the ALMA detections and estimate their radius, mass and number density. In Section 5, we use numerical simulations of starless core evolution to create synthetic observations to predict the expected number of starless core detections in our dataset, under the turbulent fragmentation model. In Section 6, we consider our results in the context of similar ALMA observations of Chamaeleon I (Dunham et al., 2016) and Ophiuchus (Kirk et al., 2017a), and run a simple virial analysis to explore whether differences in core boundedness is a plausible explanation for the varied levels of agreement from the turbulent fragmentation model. We summarize our findings in Section 7.

Chapter 2

ALMA Observations

2.1 Target Selection: SCUBA

In their re-analysis of all SCUBA archive data of the Orion star-forming regions, Nutter & Ward-Thompson (2007) (hereafter NWT07) identified a total of 393 dense cores in the Orion molecular cloud complex. The detected cores were classified as protostellar or starless using archival data from the Spitzer Space Telescope. In the Orion B North portion of the complex, covering the area of NGC 2068/2071, 73 of the 100 dense cores were classified as starless (NWT07). The NWT07 catalog is sensitive down to a mass of $0.1 M_{\odot}$ and maps the entirety of the NGC 2068/2071 star forming regions. We obtained ALMA Cycle 3 observations observations of all 73 starless cores identified by NWT07 in the Orion B North region. Figure 2.1 shows the 73 ALMA pointings overlaid on a more recent SCUBA-2 850 μm image of Orion BN presented by Kirk et al. (2016), and positional information is given in Table 2.1.

2.2 ALMA Data

The ALMA Band 3 data were observed between 2016 March 08 and 2016 August 27, and consisted of 7 unique observation times, using an average of 38 antennas. Four spectral windows were used, with three configured for continuum measurements, centered at 101 GHz, 103 GHz, and 113 GHz, each with a bandwidth of 1875 MHz. The total continuum bandwidth is therefore approximately 6 GHz at a central frequency of 106 GHz. The last spectral window was configured for observation of ^{12}CO $(1-0)$ emission at 115 GHz. Our main focus in this study is the continuum data; we use the CO line data appropriately when needed (see Section 3.2 for details).

Flux and bandpass calibrators were observed at the beginning of each execution block,

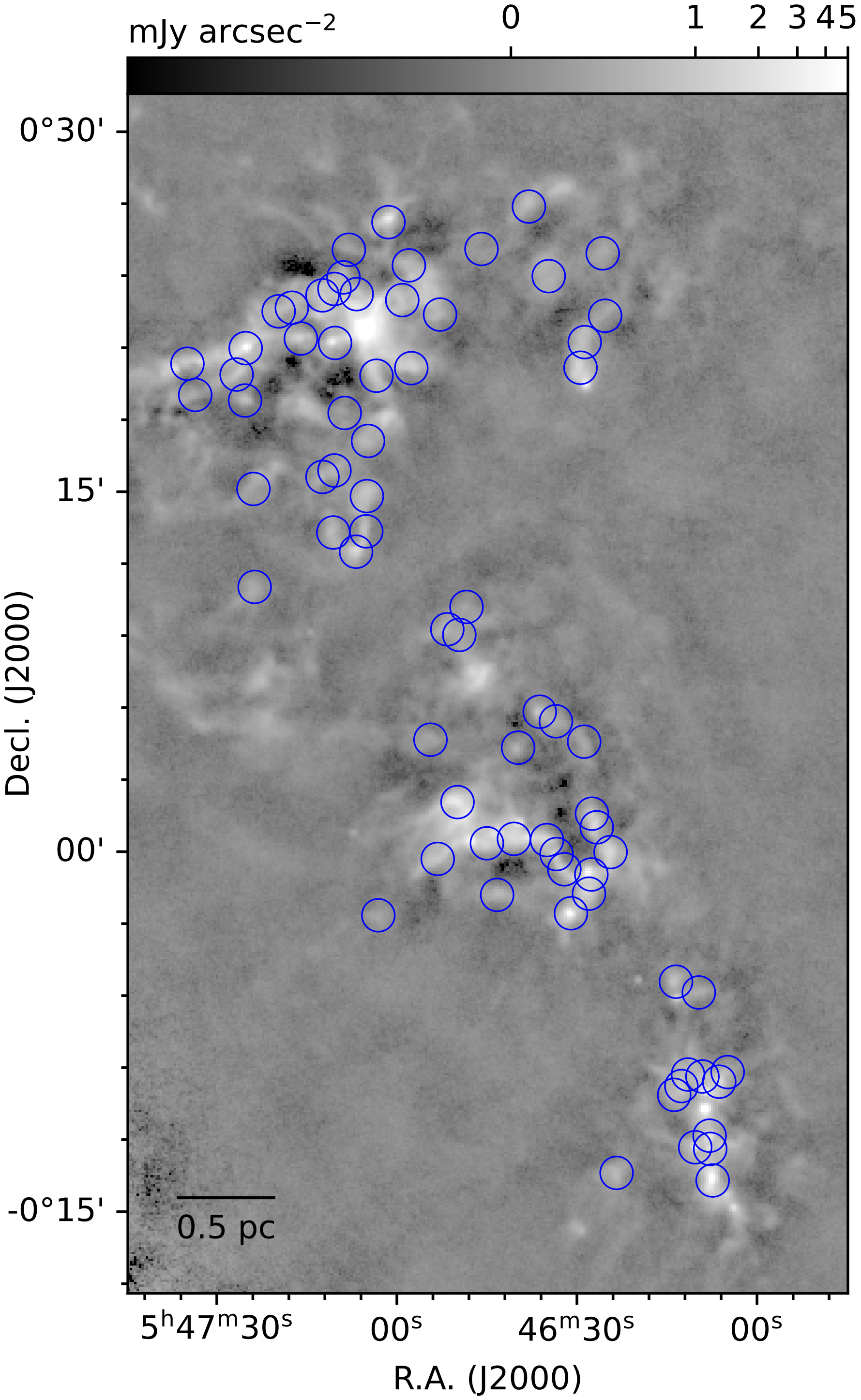

Figure 2.1: SCUBA-2 850 μm image of the Orion BN cloud adapted from Kirk et al. (2016). The blue circles show all 73 *starless* dense cores identified by NWT07 which were observed by ALMA, with the diameters of the circles equal to the FWHM of the primary beam of the 12m observations.

followed by single pointings of all 73 science targets, with periodic phase gain calibrators therein. Most sources (50) were observed during all 7 execution blocks, totalling 270 seconds of on source time, with the remaining (23) sources missing the last execution block, totalling 230 seconds of on-source time. These continuum observations were requested to have a 1σ rms noise of 0.07 mJy beam^{-1}, and was achieved for all ALMA pointings (see Table 2.1 and below for details).

The array was in a relatively compact configuration for the first five observation windows (C-2/3), with antenna separations ranging from approximately 15 m to 460 m. In the final two observations, the array was in a slightly more expanded configuration (C-4/5) with antenna separations ranging from approximately 15 m to 1125 m. This yields an average synthesized beam of $1.5'' \times 1.3''$ at a position angle of 75 degrees, along with a maximum recoverable scale of approximately $14''$. There is no significant difference in the synthesized beam between sources that were only observed for 230 seconds, and those observed for the full 270 seconds.

The calibration and reduction was conducted in the pipeline version 4.7.0 of the Common Astronomy Software Applications (CASA) software. For imaging and analysis, CASA version 6.5.0 was utilized for its refined automasking routines (The CASA Team et al., 2022).

For continuum imaging, the line emission was first subtracted, along with these standard choices of imaging parameters: Briggs weighting (with a robust value of $R = 0.5$), a uvtaper of 0.8 arcsec to reduce sidelobe contamination, and default automasking parameters. Self-calibration routines were performed on the continuum where it improved image quality, which in our case was where the peak emission was above approximately 10 mJy beam^{-1}. This brought all fields to the rms noise level requested for the observations, 0.07 mJy beam^{-1}. In the case where the field of view of individual ALMA observations overlapped, mosaicking was conducted (prior to self-calibration where appropriate) to improve the final sensitivity of the image. The observations lying within a mosaicked area are noted in Table 2.1.

For line emission imaging, the continuum was first subtracted, along with only one change with respect to the above parameters, a modified version of the Briggs weighting scheme called `briggsbwtaper`, with the same robust value of $R = 0.5$. The purpose with this choice in weighting scheme is to modify the cube imaging weights to have a similar density to that of the continuum imaging weights (The CASA Team et al., 2022), which gave the best results in our images. We use this data as a indicator for protostellar nature, as the data achieves a sensitivity of 1.1 K in a 0.5 km s^{-1} channel, which is sufficient to detect outflow signatures, if any are present near our identified detections.

Table 2.1: Noise Levels of Targeted ALMA Observations

Field[a]	R.A. (J2000)	Decl. (J2000)	ALMA Mosaic Field[b]	1σ rms[c] (mJy beam^{-1})	Int. Time[d] (s)	YSO[e]
BN-546049-00911	05:46:04.90	-00:09:11.00	BN-546049-00911Mosaic	0.045	270	N
BN-546063-00935	05:46:06.30	-00:09:35.00	BN-546049-00911Mosaic	0.045	270	Y
BN-546074-01342	05:46:07.40	-00:13:42.00	BN-546074-01342Mosaic	0.061	270	Y
BN-546078-01223	05:46:07.80	-00:12:23.00	BN-546074-01342Mosaic	0.061	270	Y
BN-546079-01150	05:46:07.90	-00:11:50.00	BN-546074-01342Mosaic	0.061	270	Y
BN-546091-00922	05:46:09.10	-00:09:22.00	BN-546049-00911Mosaic	0.045	270	N
BN-546097-00552	05:46:09.70	-00:05:52.00	BN-546097-00552Mosaic	0.054	270	N
BN-546103-01219	05:46:10.30	-00:12:19.00	BN-546074-01342Mosaic	0.061	270	Y
BN-546115-00917	05:46:11.50	-00:09:17.00	BN-546049-00911Mosaic	0.045	270	N
BN-546126-00946	05:46:12.60	-00:09:46.00	BN-546049-00911Mosaic	0.045	270	N
BN-546135-00525	05:46:13.50	-00:05:25.00	BN-546097-00552Mosaic	0.054	270	Y
BN-546138-01008	05:46:13.80	-00:10:08.00	BN-546049-00911Mosaic	0.045	270	N
BN-546234-01323	05:46:23.40	-00:13:23.00	...	0.050	270	N
BN-546244-00001	05:46:24.40	-00:00:01.00	BN-546244-00001Mosaic	0.054	270	N
BN-546253+02220	05:46:25.30	+00:22:20.00	...	0.053	230	N
BN-546257+02456	05:46:25.70	+00:24:56.00	...	0.057	230	N
BN-546267+00101	05:46:26.70	+00:01:01.00	BN-546244-00001Mosaic	0.054	270	N
BN-546275+00135	05:46:27.50	+00:01:35.00	BN-546244-00001Mosaic	0.054	270	N
BN-546276-00057	05:46:27.60	-00:00:57.00	BN-546244-00001Mosaic	0.076*	270	Y
BN-546280-00145	05:46:28.00	-00:01:45.00	BN-546244-00001Mosaic	0.054	270	N
BN-546287+02114	05:46:28.70	+00:21:14.00	BN-546287+02114Mosaic	0.055	230	N
BN-546288+00435	05:46:28.80	+00:04:35.00	...	0.047	270	N

to be continued on the next page

Table 2.1: (continued from previous page)

Field[a]	R.A. (J2000)	Decl. (J2000)	ALMA Mosaic Field[b]	1σ rms[c] (mJy beam^{-1})	Int. Time[d] (s)	YSO[e]
BN-546294+02010	05:46:29.40	+00:20:10.00	BN-546287+02114Mosaic	0.055	230	N
BN-546310-00234	05:46:31.00	-00:02:34.00	BN-546244-00001Mosaic	0.054	270	Y
BN-546321-00044	05:46:32.10	-00:00:44.00	BN-546244-00001Mosaic	0.054	270	N
BN-546334-00006	05:46:33.40	-00:00:06.00	BN-546244-00001Mosaic	0.054	270	Y
BN-546335+00526	05:46:33.50	+00:05:26.00	BN-546335+00526Mosaic	0.047	270	N
BN-546347+02359	05:46:34.70	+00:23:59.00	...	0.056	230	N
BN-546350+00029	05:46:35.00	+00:00:29.00	BN-546244-00001Mosaic	0.054	270	N
BN-546362+00550	05:46:36.20	+00:05:50.00	BN-546335+00526Mosaic	0.047	270	N
BN-546380+02653	05:46:38.00	+00:26:53.00	...	0.060	230	N
BN-546398+00420	05:46:39.80	+00:04:20.00	...	0.048	270	Y
BN-546405+00032	05:46:40.50	+00:00:32.00	BN-546405+00032Mosaic	0.050	270	N
BN-546433-00148	05:46:43.30	-00:01:48.00	...	0.054	270	N
BN-546450+00021	05:46:45.00	+00:00:21.00	BN-546405+00032Mosaic	0.050	270	N
BN-546459+02507	05:46:45.90	+00:25:07.00	...	0.059	230	N
BN-546484+01012	05:46:48.40	+00:10:12.00	BN-546484+01012Mosaic	0.042	270	N
BN-546496+00902	05:46:49.60	+00:09:02.00	BN-546484+01012Mosaic	0.042	270	N
BN-546499+00204	05:46:49.90	+00:02:04.00	...	0.049	270	N
BN-546516+00916	05:46:51.60	+00:09:16.00	BN-546484+01012Mosaic	0.042	270	N
BN-546528+02223	05:46:52.80	+00:22:23.00	...	0.054	230	N
BN-546532-00018	05:46:53.20	-00:00:18.00	...	0.051	270	N
BN-546544+00440	05:46:54.40	+00:04:40.00	...	0.047	270	N
BN-546576+02009	05:46:57.60	+00:20:09.00	...	0.054	230	N
BN-546580+02426	05:46:58.00	+00:24:26.00	...	0.058	230	N

to be continued on the next page

Table 2.1: (continued from previous page)

Field[a]	R.A. (J2000)	Decl. (J2000)	ALMA Mosaic Field[b]	1σ rms[c] (mJy beam^{-1})	Int. Time[d] (s)	YSO[e]
BN-546591+02259	05:46:59.10	+00:22:59.00	...	0.055	230	N
BN-547014+02614	05:47:01.40	+00:26:14.00	...	0.059	230	Y
BN-547031-00239	05:47:03.10	-00:02:39.00	...	0.053	270	N
BN-547034+01950	05:47:03.40	+00:19:50.00	...	0.054	270	N
BN-547048+01707	05:47:04.80	+00:17:07.00	...	0.050	270	N
BN-547050+01449	05:47:05.00	+00:14:49.00	...	0.049	270	N
BN-547051+01321	05:47:05.10	+00:13:21.00	BN-547051+01321Mosaic	0.050	270	N
BN-547067+02314	05:47:06.70	+00:23:14.00	BN-547067+02314Mosaic	0.049	230	N
BN-547068+01230	05:47:06.80	+00:12:30.00	BN-547051+01321Mosaic	0.050	270	N
BN-547080+02505	05:47:08.00	+00:25:05.00	BN-547067+02314Mosaic	0.049	230	N
BN-547087+01817	05:47:08.70	+00:18:17.00	...	0.052	270	N
BN-547089+02356	05:47:08.90	+00:23:56.00	BN-547067+02314Mosaic	0.049	230	N
BN-547103+02112	05:47:10.30	+00:21:12.00	...	0.066	230	Y
BN-547104+01553	05:47:10.40	+00:15:53.00	BN-547104+01553Mosaic	0.045	270	N
BN-547104+02327	05:47:10.40	+00:23:27.00	BN-547067+02314Mosaic	0.049	230	Y
BN-547106+01318	05:47:10.60	+00:13:18.00	BN-547051+01321Mosaic	0.050	270	N
BN-547124+01537	05:47:12.40	+00:15:37.00	BN-547104+01553Mosaic	0.045	270	N
BN-547124+02311	05:47:12.40	+00:23:11.00	BN-547067+02314Mosaic	0.049	230	N
BN-547160+02123	05:47:16.00	+00:21:23.00	BN-547160+02123Mosaic	0.048	230	Y
BN-547175+02240	05:47:17.50	+00:22:40.00	BN-547160+02123Mosaic	0.048	230	N
BN-547197+02231	05:47:19.70	+00:22:31.00	BN-547160+02123Mosaic	0.048	230	N
BN-547237+01102	05:47:23.70	+00:11:02.00	...	0.048	270	N
BN-547239+01507	05:47:23.90	+00:15:07.00	...	0.051	270	N

to be continued on the next page

Table 2.1: (continued from previous page)

Field[a]	R.A. (J2000)	Decl. (J2000)	ALMA Mosaic Field[b]	1σ rms[c] (mJy beam^{-1})	Int. Time[d] (s)	YSO[e]
BN-547252+02059	05:47:25.20	+00:20:59.00	BN-547252+02059Mosaic	0.055	230	Y
BN-547253+01848	05:47:25.30	+00:18:48.00	BN-547252+02059Mosaic	0.055	270	N
BN-547267+01953	05:47:26.70	+00:19:53.00	BN-547252+02059Mosaic	0.055	230	N
BN-547336+01902	05:47:33.60	+00:19:02.00	BN-547336+01902Mosaic	0.054	270	N
BN-547349+02020	05:47:34.90	+00:20:20.00	BN-547336+01902Mosaic	0.054	230	N

[a] Observed SCUBA core name from Nutter & Ward-Thompson (2007).

[b] For individual fields which overlap in coverage, the mosaic field name is given (taken to be the eastern-most field).

[c] 1σ root-mean-square noise, computed in non-detection areas of the field. This computation was performed on the non-primary beam corrected image.

[d] Total integration time on the individual field.

[e] Protostellar classification based on more recent catalogs studied (see Section 3.1 for details).

* Due to a bright central protostellar source, we report a more representative value of rms for this individual field, as opposed to the rms value computed for the mosaicked field.

Chapter 3

Dense Core Properties and Protostellar Associations

All final images produced were corrected for primary beam attenuation. We subsequently use CASA's `imfit` task to fit elliptical Gaussians to all continuum sources found. We detect a total of 34 continuum sources across 19 individual ALMA pointings. Table 3.1 lists each of the continuum sources with a running index number, location information based on the center of the two-dimensional Gaussian fit and additional associated statistics. These include the peak emission, the total flux, the major and minor axes, as well as the position angle. We also show the deconvolved values (and their uncertainties) for the size, and positional angle; with a -1 indicator if partially or fully unresolved.

Of the 34 sources detected, 16 are found within the central potion of the primary beam (here defined to be 14″ away from the center, the beamsize of the NWT07 catalog), while the remaining 18 sources were located well away from the center and as such are less likely to be the intended target core.

3.1 Protostellar Associations

As introduced in Section 2.1, NWT07 identified 73 starless core candidates in their re-analysis of all SCUBA archival data in the Orion B North region. Since this time, there have been many studies of protostellar sources in the Orion molecular cloud complex, which have revealed many previously unknown protostars. Our observations will easily detect protostellar sources, and due to the statistical nature of our analysis, an accurate measure of the starless core population is needed. We have examined a number of different catalogs to check for any protostellar sources, which can be associated with our 34 ALMA detections, spanning from the radio to near-infrared wavelengths. Table 3.2 lists each of our 34 ALMA detections along with each nearest protostellar source in all of the catalogs studied.

In summary, all but 5 of our ALMA detections are directly associated with a protostellar source, with one of those showing signs of protostellar outflow in the CO data (see Section 3.2 for details). The results from our protostellar catalog searches, as they pertain to the 34 ALMA detections are detailed in the following sections.

We perform an analogous check for the original starless core population identified by NWT07 for use in our statistical analysis (see Section 3.3 for details).

3.1.1 Associations with Spitzer YSOs

We first search for the nearest Spitzer YSO in the Megeath et al. (2012) catalog. The separations found with this catalog fall into two main domains, those with very small separations ($< 2''$), and those with larger separations ($> 13''$). There are three such detections which lie in moderate separation range, source 23, 24, and 27, with a separation of $4.5''$, $5.3''$, and $7.8''$ to the nearest Spitzer YSO, respectively. Of these three Spitzer YSOs, the two near ALMA sources 23 and 24 are already more directly associated with other ALMA detections. The additional catalogues examined later in this section provided clarity on the protostellar/starless classification for these three detections.

In this study, we classify separations of less than 2 arcsec to the nearest Spitzer YSO to be coincident detections. In total, we find that 27 of our ALMA detections are found in the Spitzer catalog and we subsequently classify these detections as protostellar in nature.

3.1.2 Associations with ALMA-based Catalogs

We compared our detections to those found in Tobin et al. (2020), The VLA/ALMA Nascent Disk and Multiplicity (VANDAM) Survey of Orion Protostars. This survey population was drawn from the Herschel Orion Protostellar Survey (HOPS) (specifically Fischer et al., 2010; Stutz et al., 2013; Furlan et al., 2016), where all Class 0, Class 1 and Flat Spectrum protostars (with additional constraints) were selected for observations with ALMA Band 7 (0.87mm), at a resolution of 0.1 arcsec (40 AU), and with the VLA at 9 mm at a resolution of 0.08 arcsec (32 AU). The VANDAM study observed a total of 328 protostars with ALMA, and only 148 protostars with the VLA (Tobin et al., 2020), so we choose to perform our association verification with the published ALMA catalog. Additional visual checks with both catalogs were conducted to ensure that associations in the Orion B North region were not missed. Compared to our ALMA data, the VANDAM observations have a higher angular resolution and reduced ability to recover flux on larger angular scales, hence VANDAM is expected to only detect protostellar sources.

We find that 27 of 34 detections lie within VANDAM coverage, but only 25 detections were directly observed, with separations of no more than 0.50 arcsec. Two of our ALMA detections, namely source 23 and 24, are undetected in the VANDAM observations, and therefore should be starless. The remaining 5 ALMA detections were not found to lie within any VANDAM observation, and as such, have no associations from this catalog.

Additionally, we compare our detections to the 19 sources analyzed by Dutta et al. (2020) in the Orion B region, through the ALMA Survey of Orion Planck Galactic Cold Clumps (ALMASOP). These are ALMA Band 6 (1.3mm) observations, with a resolution of 0.35 arcsec (140 AU). Nine of our detections are found in the ALMASOP survey, with separations less than approximately 0.5 arcsec, eight of which are classified as protostellar. These same eight sources are also identified as protostars by the VANDAM survey (Tobin et al., 2020). The one remaining ALMASOP associated detection, G205.46-14.56M3, is classified as starless by ALMASOP, in agreement with our final classification of source 1.

3.1.3 Other Published Catalogs

The following catalogs were also parsed for potential protostellar matches: the Herschel Gould Belt Survey (Könyves et al., 2020), the aforementioned Herschel Orion Protostellar Survey (HOPS) (Stutz et al., 2013; Furlan et al., 2016), the VISTA Orion Mini-Survey (Spezzi et al., 2015), the Spitzer Extended Solar Neighborhood Archive (SESNA) (Gutermuth, in prep) and the Wide-field Infrared Survey Explorer (WISE) all-sky catalog (Marton et al., 2016). No new protostellar candidates were identified based on these catalogues, but the associations that we find are included in Table 3.2 for completeness.

3.2 ALMA CO Data

As introduced in Section 2.2, one spectral window of our ALMA observations was configured for observations of ^{12}CO $(1-0)$ emission at 115 GHz. We utilize the ^{12}CO data to search for protostellar outflow signatures around the 5 ALMA detections which had no protostellar associations, as identified in Section 3.1. In summary, we find evidence for a protostellar outflow signature in only one of our imaged fields near source 5.

As shown in Figure 3.1, source 5 shows red shifted and blue shifted CO emission perpendicular to the orientation of what appears to be a region of extended emission. Source 5 also contains two nearby protostellar sources found through the VISTA survey (Spezzi et al., 2015). The upper source, 054607.227-001134.91, is approximately 15$''$ away from our detection, and is labeled as a Class II source (Spezzi et al., 2015), and was previously found by Flaherty & Muzerolle (2008) and Fang et al. (2009). The lower source, 054607.884-001156.83,

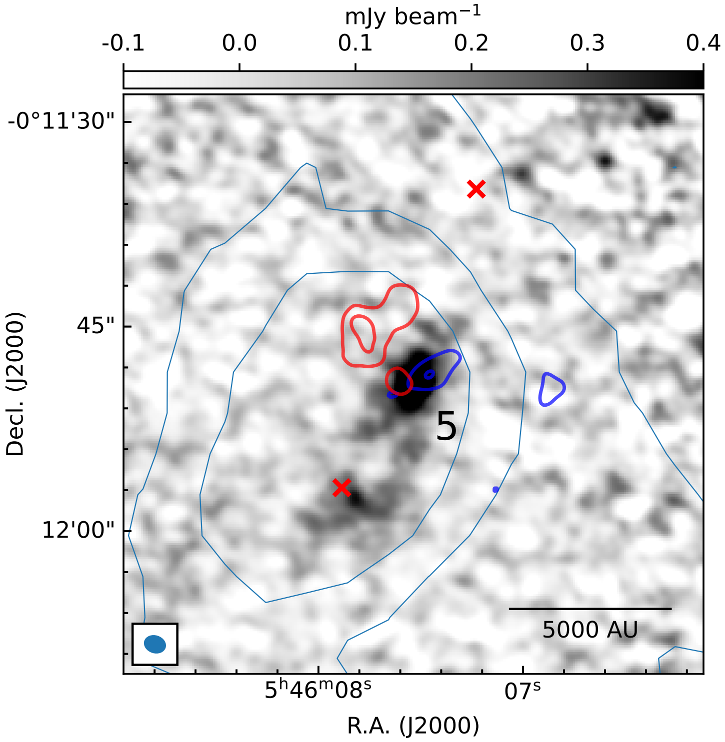

Figure 3.1: Zoom-in of the upper region of ALMA field BN-546074-01342Mosaic, as given in Figure 3.2, with source 5 shown in the center. The grayscale ranges linearly from -0.1 mJy beam^{-1} to 0.6 mJy beam^{-1}, and the synthesized beam is given in the lower left corner. The light blue contours correspond to SCUBA2 850 μm emission at the corresponding levels in mJy arcsec^{-2}: 0.15, 0.5, 1.0, 1.5, 3.0, 5.0. Protostellar sources in the field of view are plotted with red x's. The blue and red contours represented velocity-shifted components of ^{12}CO $(1-0)$; these are at $3, 5\sigma$ where the noise is $1\sigma \sim 0.164$Jy beam^{-1} km s^{-1}.

is approximately 9″ away from our detection, and is labeled as a potential Class III source (Spezzi et al., 2015).

This nearby protostellar source appears to lie along a region of extended emission, to the southwest of our ALMA detection. The extended emission features in our ALMA observations are very low-level, even with the inclusion and combination of our ACA data (not shown here), only reaching slightly above 1σ. Nonetheless these low-level features may be indicative of streamer-like objects spanning thousands of AU, recently seen in other star forming systems (e.g., Pineda et al., 2020; Murillo et al., 2022; Pineda et al., 2023) or an envelope associated with filamentary structure (e.g., Tobin et al., 2010). We do not pursue further analysis of this potential extended emission here.

3.3 Associations Summary

After consideration of the protostellar catalogs studied, with the additional of our ALMA observations in the CO, we classify sources sources 1, 4, 23, and 24 as likely being starless. In addition to this final classification of our candidate starless cores, we visually verified all multi-wavelength images from both Spitzer and Herschel, and found no indications of protostellar sources in those locations. The details of our associations are listed in Table 3.2, and explained in greater detail in the following section.

As some analysis is dependent on accurate classification of the original NWT07 dense core population (see Section 4.3 for example), we perform the same check on that catalog for protostellar associations. We classify any protostellar object lying within 14″ of the peak of the NWT07 core as associated, based on the beamsize of the SCUBA catalog. A total of 15 NWT07 SCUBA cores are re-classified as protostellar based on the catalogs studied, and will be used throughout the analysis when needed. In summary, we find that 58 fields are truly starless after verifying all ancillary data. This information is presented in Table 2.1, in the final column.

3.4 Candidate Starless Core Detections

Now we examine each of the four ALMA starless core detections in turn. Figure 3.2 shows starless core candidate source 4, and all other protostellar cores which lie in the same mosaic. This source is one of the dimmest sources detected in our sample, with a peak flux measurement of 0.45 mJy beam^{-1}, and has a detection significance of 7.4 times the local rms noise. This source is found to the south of multiple other protostellar sources in the SCUBA core BN-546074-01342, which have been positively identified as protostellar by Tobin et al. (2020) (see Table 3.2 for details).

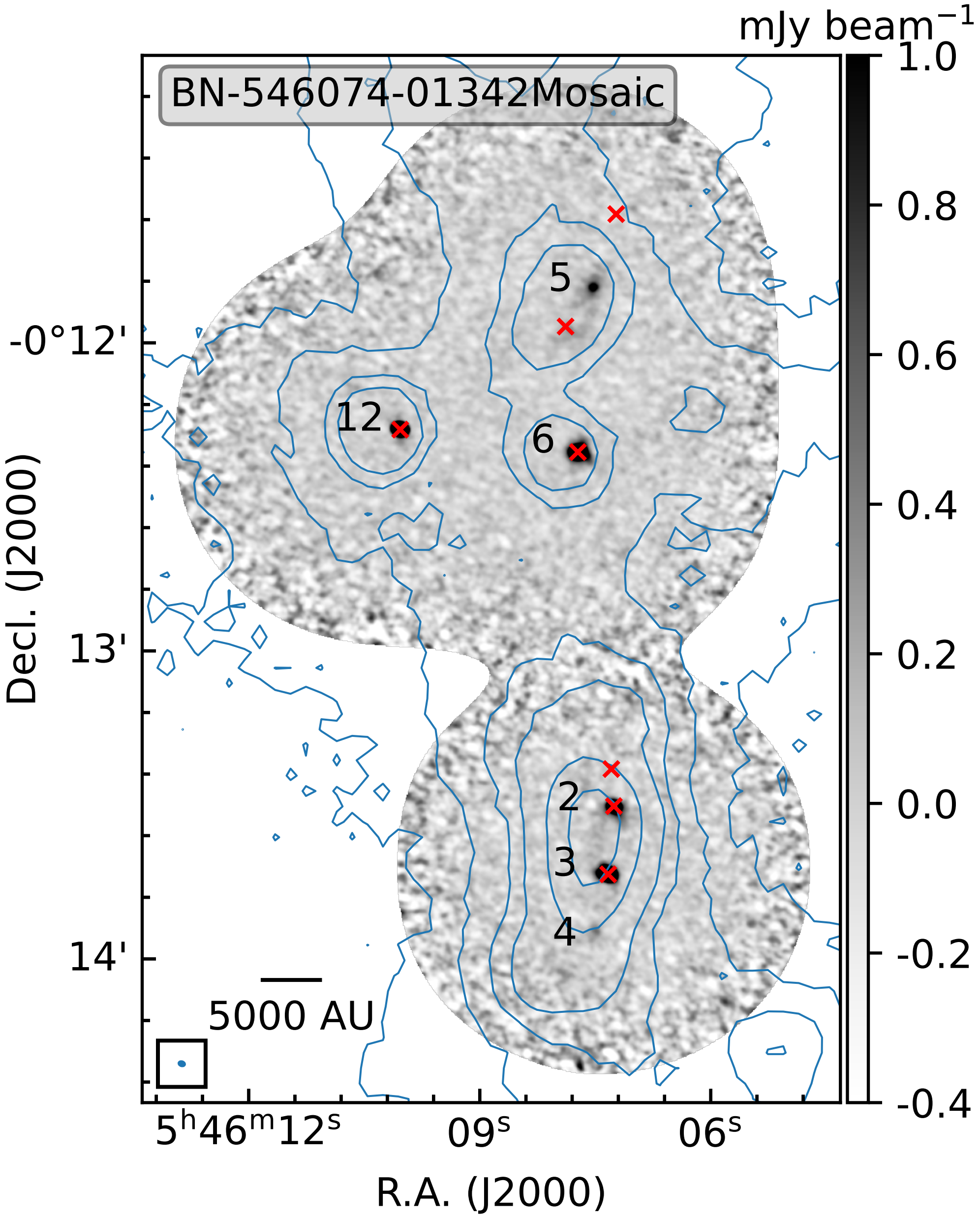

Figure 3.2: ALMA field BN-546074-01342Mosaic, with starless candidate sources 4. The grayscale ranges linearly from -0.5 mJy beam^{-1} to 1.0 mJy beam^{-1}. The blue contours correspond to SCUBA-2 850 μm emission at the corresponding levels in mJy arcsec^{-2}: 0.15, 0.5, 1.0, 1.5, 3.0, 5.0. All detections are labeled in black with their respective index number. Protostellar sources in the field of view are also plotted with red markers (see Table 3.2 for details). The synthesized beam is plotted in the lower left corner, along with a scalebar, indicating a linear distance of 5000 AU, at the assumed distance to Orion of 419 pc.

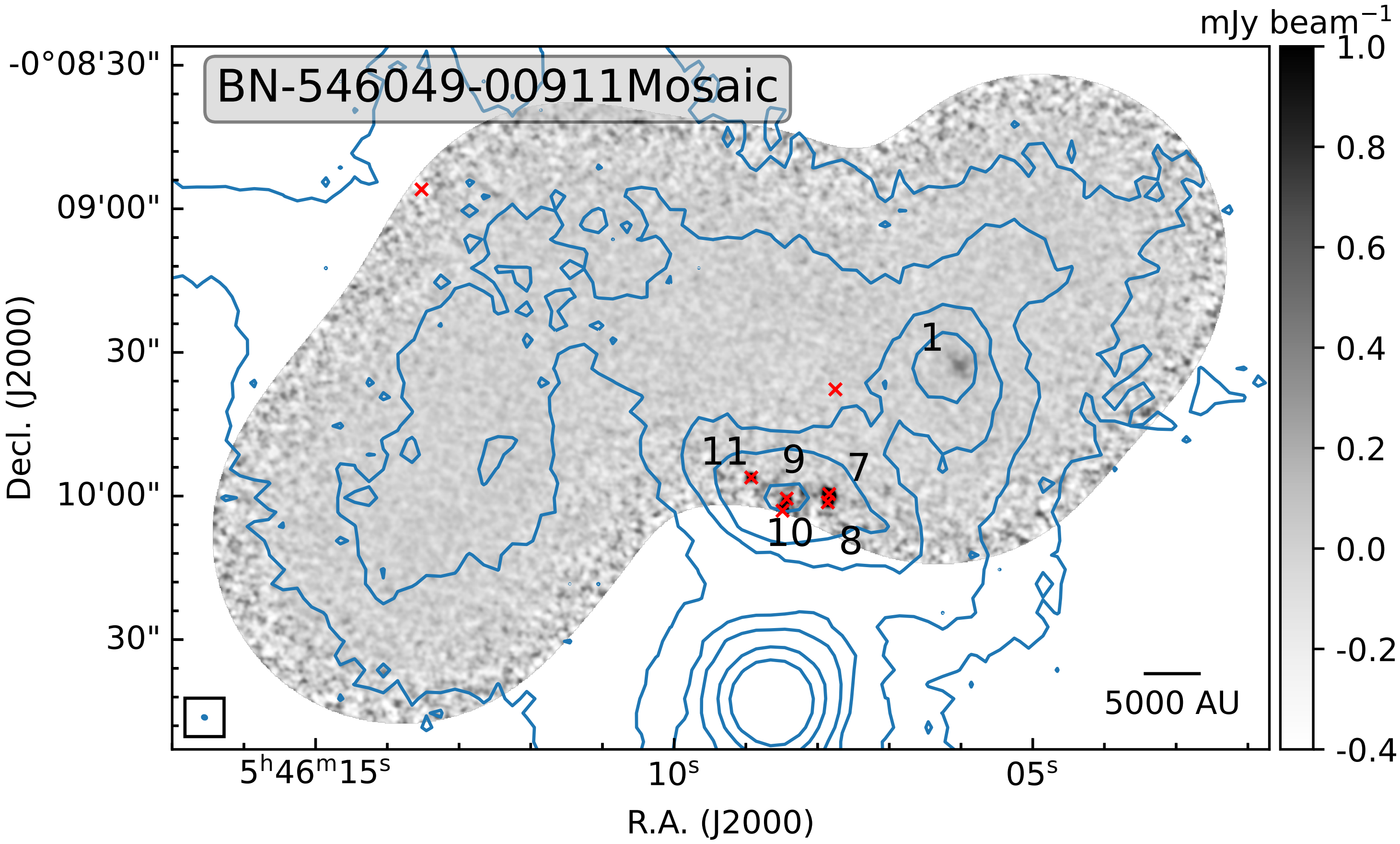

Figure 3.3: ALMA field BN-546049-00911Mosaic, with starless candidate source 1. See Figure 3.2 for plotting conventions.

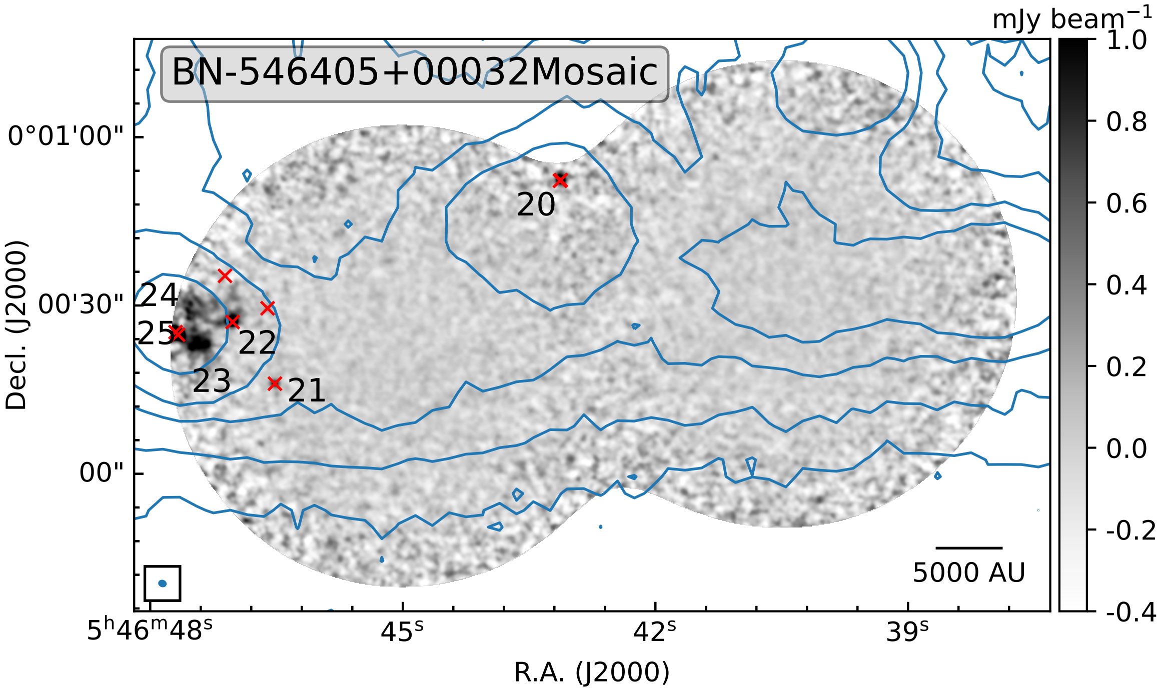

Figure 3.4: ALMA field BN-546405+00032Mosaic, with starless candidates sources 23 and 24. See Figure 3.2 for plotting conventions.

Figure 3.3 shows source 1, the only candidate starless core detection that is centered on a SCUBA-based target. This detection lies in the central portion of the SCUBA dense core BN-546063-00935 (NWT07) and has a detection significance of 8 times the local rms noise. The area surrounding the peak position of the detection is quite extended, and forms a larger area of diffuse emission. As highlighted in Section 3.1.2, our source 1 is associated with the ALMASOP core G205.46-14.56M3 (G205-M3). G205-M3 is the only core in the ALMASOP dataset that shows signatures of fragmenting substructure at a scale of 1000 AU (Sahu et al., 2021). The emission is resolved into two noticeable substructures with diameters of 1755 AU and 820 AU, and are approximately separated by a distance of 1200 AU (Sahu et al., 2021). Sahu et al. (2021) find that the enclosed masses, and their respective density profiles, are not consistent with a BE sphere-like model, and argue that this system likely represents an evolved starless state, just before the onset of star formation.

Figure 3.4 shows source 23 and 24, two detections found within an area undergoing a large amount of fragmentation. These detections are located quite offset from the center of the NWT07 dense core BN-546450+00021. The larger area surrounding this dense core is home to faint and complex emission structure, and more sensitive recent observations conducted by Kirk et al. (2016), indicate that there is a dense core associated with the positions of sources 23 and 24, with many individual fragmenting components[1]. Note that the VANDAM (protostar) survey did cover the full region with ALMA, but did not detect any emission for source 23 and 24. On the other hand, a recent 350GHz ACA Survey of 300 protostellar sources identified from the Herschel Orion Protostellar Survey was conducted by Federman et al. (2023). These observations trace the protostellar flux at the envelope scale ($\leq$ 8000 AU), and we find extended continuum detections at the locations of our source 23 and 24 (Federman et al., 2023). Thus, this region could very likely be a moment in time where the transition from the starless core stage into the protostellar stage is being directly observed and currently ongoing.

---

[1] See Appendix A.1 regarding the differences between the SCUBA and SCUBA-2 core catalogs for Orion BN.

Table 3.1: Observed Properties of ALMA Detections

Scr	R.A.	Decl.	Pk^{a}	Pk$_{err}{}^{a}$	Tot^{a}	Tot$_{err}{}^{a}$	FWHM$_{a}{}^{a}$	FWHM$_{b}{}^{a}$	P.A.^{a}	FWHM$_{a,d}{}^{b}$ (arcsec)		FWHM$_{b,d}{}^{b}$ (arcsec)		P.A.$_{d}{}^{b}$ (deg)	
	(J2000)	(J2000)	(mJy beam^{-1})		(mJy)		(arcsec)		(deg)	fit	err	fit	err	fit	err
1	05h46m06.01s	-00d09m32.70s	0.36	0.08	4.60	1.03	5.471	4.622	58.8	5.26	1.22	4.43	1.07	58	53
2	05h46m07.26s	-00d13m30.27s	9.48	0.16	12.22	0.33	1.849	1.511	71.2	0.84	0.09	0.74	0.08	65	66
3	05h46m07.33s	-00d13m43.49s	31.37	0.16	36.88	0.31	1.779	1.433	70.1	0.68	0.03	0.56	0.03	57	12
4	05h46m07.51s	-00d13m54.79s	0.45	0.16	1.36	0.63	2.978	2.177	162.1	2.67	1.19	1.42	1.04	162	42
5	05h46m07.53s	-00d11m49.22s	0.97	0.14	5.25	0.90	4.345	2.694	152.4	4.14	0.74	2.14	0.49	153	11
6	05h46m07.73s	-00d12m21.27s	14.37	0.17	21.73	0.38	1.977	1.658	82.8	1.15	0.06	0.94	0.06	110	12
7	05h46m07.84s	-00d09m59.61s	6.45	0.11	7.59	0.21	1.726	1.361	65.2	0.81	0.07	0.36	0.10	62	8
8	05h46m07.86s	-00d10m01.33s	2.74	0.11	3.44	0.23	1.754	1.427	63.0	0.88	0.17	0.56	0.23	57	48
9	05h46m08.42s	-00d10m01.03s	0.86	0.09	5.53	0.69	4.752	2.702	38.9	4.52	0.60	2.33	0.34	38	8
10	05h46m08.49s	-00d10m03.10s	8.13	0.10	7.55	0.17	1.444	1.284	83.2	-1.00	-1.00	-1.00	-1.00	-1	-1
11	05h46m08.92s	-00d09m56.11s	2.07	0.11	2.28	0.20	1.576	1.392	73.8	0.51	0.31	0.36	0.21	129	73
12	05h46m10.04s	-00d12m16.83s	39.04	0.15	40.36	0.28	1.657	1.352	72.0	0.31	0.03	0.19	0.09	165	24
13	05h46m13.13s	-00d06m04.94s	9.41	0.14	11.18	0.27	1.655	1.379	67.3	0.71	0.07	0.50	0.08	60	19
14	05h46m14.20s	-00d05m26.71s	0.51	0.13	0.54	0.24	1.704	1.177	80.5	-1.00	-1.00	-1.00	-1.00	-1	-1
15	05h46m27.91s	-00d00m52.11s	65.62	0.14	73.72	0.27	1.662	1.409	74.0	0.52	0.02	0.49	0.02	43	26
16	05h46m28.34s	+00d19m49.18s	1.47	0.14	1.79	0.28	1.816	1.387	78.5	0.93	0.36	0.42	0.27	77	82
17	05h46m28.61s	+00d20m58.08s	0.50	0.13	0.49	0.23	1.675	1.212	127.5	0.00	1.59	0.00	0.60	-1	-1
18	05h46m30.91s	-00d02m35.07s	7.55	0.15	17.54	0.47	2.456	1.972	63.7	1.89	0.07	1.45	0.06	58	7
19	05h46m31.09s	-00d02m32.95s	16.15	0.15	25.05	0.35	1.862	1.736	151.5	1.31	0.03	0.73	0.05	160	5
20	05h46m43.12s	+00d00m52.47s	1.70	0.13	2.40	0.28	1.759	1.619	2.1	1.15	0.33	0.56	0.42	169	36
21	05h46m46.52s	+00d00m16.09s	1.00	0.12	1.04	0.22	1.532	1.370	63.8	0.00	1.05	0.00	0.50	-1	-1
22	05h46m47.03s	+00d00m27.20s	1.96	0.13	3.55	0.34	2.212	1.652	109.8	1.69	0.25	0.83	0.30	118	13
23	05h46m47.43s	+00d00m23.24s	1.10	0.09	12.48	1.10	5.314	4.321	37.9	5.11	0.47	4.09	0.39	36	22
24	05h46m47.51s	+00d00m29.50s	0.85	0.10	7.75	1.04	5.548	3.319	9.5	5.38	0.75	2.97	0.45	9	9
25	05h46m47.69s	+00d00m25.02s	5.38	0.13	7.22	0.27	1.810	1.496	53.6	1.01	0.11	0.64	0.13	37	15
26	05h46m47.97s	+00d01m41.80s	1.10	0.13	2.55	0.42	2.665	1.684	38.5	2.24	0.48	0.99	0.43	34	15
27	05h46m57.30s	+00d23m57.94s	3.39	0.16	4.25	0.33	1.666	1.417	72.1	0.83	0.21	0.55	0.34	61	72
28	05h47m00.92s	+00d26m21.98s	2.65	0.16	9.34	0.71	2.782	2.363	161.4	2.46	0.21	1.87	0.19	163	15
29	05h47m01.31s	+00d26m23.09s	4.91	0.17	6.96	0.37	1.784	1.484	92.6	1.05	0.12	0.72	0.13	99	21
30	05h47m10.61s	+00d21m13.78s	12.17	0.16	16.31	0.35	1.755	1.491	83.6	0.93	0.06	0.70	0.06	94	12
31	05h47m15.95s	+00d21m22.89s	2.02	0.13	2.70	0.28	1.805	1.553	89.0	0.92	0.29	0.75	0.51	111	77
32	05h47m24.84s	+00d20m58.98s	16.42	0.15	51.09	0.60	2.773	2.400	133.8	2.39	0.04	1.84	0.04	144	3
33	05h47m32.45s	+00d20m21.60s	5.56	0.15	7.19	0.30	1.742	1.502	98.7	0.91	0.14	0.60	0.20	129	21
34	05h47m36.56s	+00d20m05.89s	8.36	0.15	10.28	0.29	1.651	1.508	79.1	0.75	0.07	0.58	0.12	173	35

to be continued on the next page

Table 3.1: (continued from previous page)

Scr	R.A.	Decl.	Pk[a]	$\mathrm{Pk_{err}}$[a]	Tot[a]	$\mathrm{Tot_{err}}$[a]	$\mathrm{FWHM_a}$[a]	$\mathrm{FWHM_b}$[a]	P.A.[a]	$\mathrm{FWHM_{a,d}}$[b]	(arcsec)	$\mathrm{FWHM_{b,d}}$[b]	(arcsec)	$\mathrm{P.A._d}$[b]	(deg)
	(J2000)	(J2000)	(mJy beam^{-1})		(mJy)		(arcsec)		(deg)	fit	err	fit	err	fit	err

[a] Properties of the Gaussian fit to the ALMA emission: peak flux, integrated flux, major and minor axes of the FWHM, and position angle of the FWHM.

[b] Properties of the deconvolved Gaussian fit: major and minor axes of the FWHM, and position angle of the FWHM. Unresolved sources are indicated by values of -1.

Table 3.2: ALMA Detections and Nearest Protostellar Catalog Objects

Src	Spitzer		VANDAM		VISTA		SESNA		WISE		HGBS		APEX		ALMASOP	
#	Name	(″)	Name	(″)	Name	(″)	Name	(″)	Name	(″)	Name	(″)	Name	(″)	Name	(″)
1	3170	26.7	HOPS-387-A	38.5	129	40.3	J054607.76-000937.7	26.9	J054607.86-001000.8	39.8	1025	43.0	91	169.8	G205.46-14.56M2	38.5
2	3161	0.5	HOPS-358-A	0.1	132	7.2	J054607.26-001330.0	0.3	J054604.78-001416.6	59.3	1021	3.6	91	69.8	G205.46-14.56S1	0.2
3	3161	13.7	HOPS-358-B	0.2	132	20.5	J054607.26-001330.0	13.5	J054604.78-001416.6	50.5	1021	9.9	91	82.9	G205.46-14.56S1	0.2
4	3161	25.2	HOPS-358-B	11.6	132	32.0	J054607.26-001330.0	25.1	J054604.78-001416.6	46.4	1021	21.5	91	94.1	G205.46-14.56S1	11.6
5	3166	72.5	HOPS-401	32.2	14	9.2	J054607.88-001156.9	9.3	J054607.86-001000.8	108.5	1024	5.8	91	31.6	G205.46-14.56N2	32.2
6	3163	62.1	HOPS-401	0.1	14	24.6	J054607.88-001156.9	24.5	J054604.78-001416.6	123.6	1024	26.6	91	1.3	G205.46-14.56N2	0.1
7	3168	1.3	HOPS-387-A	0.2	129	2.1	J054607.85-001001.1	1.5	J054607.86-001000.8	1.3	1025	4.8	91	140.9	G205.46-14.56M2	0.1
8	3168	0.4	HOPS-387-B	0.1	129	0.4	J054607.85-001001.1	0.2	J054607.86-001000.8	0.6	1025	4.5	91	139.2	G205.46-14.56M2	1.7
9	3167	1.9	HOPS-386-B	0.5	129	8.5	J054608.47-001002.9	2.0	J054607.86-001000.8	8.3	1025	4.1	91	137.8	G205.46-14.56M2	0.5
10	3167	0.5	HOPS-386-A	0.1	129	9.6	J054608.47-001002.9	0.4	J054607.86-001000.8	9.7	1025	5.5	91	135.6	G205.46-14.56M2	2.8
11	3169	0.2	HOPS-386-C	0.1	129	17.0	J054608.94-000956.0	0.2	J054607.86-001000.8	16.6	1025	12.7	91	141.6	G205.46-14.56M2	8.7
12	3163	77.9	HOPS-402	0.0	14	37.9	J054607.88-001156.9	37.9	J054607.86-001000.8	139.8	1032	1.5	91	0.9	G205.46-14.56N1	0.1
13	3180	0.4	HOPS-388	0.2	96	32.2	J054613.14-000604.8	0.2	J054613.13-000604.8	0.2	1039	2.0	92	211.2	G205.46-14.56M2	245.9
14	3183	0.2	HOPS-320	0.1	157	0.5	J054614.22-000526.5	0.3	J054613.13-000604.8	41.4	1041	10.9	92	184.1	G205.46-14.56M2	287.2
15	3195	95.8	HOPS-403	0.1	178	95.5	J054629.55-000135.1	49.5	J054618.50-000017.8	145.2	1091	1.8	93	3.0	G205.46-14.56M2	621.4
16	3338	0.4	HOPS-331	0.2	120	200.6	J054628.34+001949.3	0.2	J054633.31+002255.5	200.7	1095	21.4	302	22.2	G205.46-14.56M2	1814.4
17	3354	0.5	HOPS-331	68.9	120	136.9	J054628.59+002058.1	0.2	J054633.31+002255.5	137.0	1095	90.4	302	91.2	G205.46-14.56M2	1883.1
18	3195	160.9	HOPS-373-B	0.2	177	4.2	J054629.55-000135.1	63.4	J054618.50-000017.8	231.2	1108	0.8	93	111.8	G205.46-14.56M2	558.7
19	3195	158.3	HOPS-373-A	0.3	177	7.1	J054629.55-000135.1	62.3	J054618.50-000017.8	232.0	1108	3.8	93	111.0	G205.46-14.56M2	561.9
20	3208	0.1	HOPS-363-A	0.1	179	63.5	J054643.11+000052.3	0.3	J054643.12+000052.2	0.2	1152	5.5	93	254.0	G205.46-14.56M2	835.0
21	3199	0.3	HOPS-322	0.1	179	13.4	J054646.51+000016.0	0.2	J054643.12+000052.2	62.3	1168	15.7	93	257.1	G205.46-14.56M2	840.5
22	3202	0.2	HOPS-389-A	0.1	179	0.0	J054647.01+000026.9	0.2	J054643.12+000052.2	63.5	1168	4.7	93	262.2	G205.46-14.56M2	853.8
23	3201	4.5	HOPS-323-B	4.0	179	7.3	J054647.69+000025.2	4.5	J054643.12+000052.2	70.7	1168	3.2	93	255.6	G205.46-14.56M2	855.1
24	3201	4.9	HOPS-323-A	5.0	179	7.9	J054647.69+000025.2	5.0	J054643.12+000052.2	69.7	1168	4.6	93	260.2	G205.46-14.56M2	860.6
25	3201	0.3	HOPS-323-A	0.3	179	10.3	J054647.69+000025.2	0.2	J054643.12+000052.2	73.6	1168	5.6	93	255.1	G205.46-14.56M2	859.1
26	3215	0.4	HOPS-389-B	75.2	179	76.0	J054647.96+000141.8	0.2	J054643.12+000052.2	88.0	1168	76.4	93	321.9	G205.46-14.56M2	919.3
27	3398	7.8	HOPS-338-B	0.2	165	40.6	J054657.35+002350.4	7.6	J054703.69+002328.8	100.0	1202	2.0	96	124.1	G205.46-14.56M2	2166.3
28	3409	1.2	HOPS-341	0.5	126	38.3	J054701.07+002544.1	38.0	J054703.69+002328.8	178.1	1202	155.7	96	277.0	G205.46-14.56M2	2320.1
29	3408	1.7	HOPS-340	0.1	126	39.5	J054701.07+002544.1	39.2	J054703.69+002328.8	177.8	1202	159.0	96	280.6	G205.46-14.56M2	2323.2
30	3359	0.4	HOPS-365	0.1	103	1.8	J054710.62+002113.8	0.1	J054710.61+002114.0	0.3	1258	1.5	96	266.7	G205.46-14.56M2	2093.5
31	3361	16.0	HOPS-347	0.2	134	16.3	J054714.89+002118.8	16.3	J054712.90+002206.6	63.0	1285	1.6	96	343.8	G205.46-14.56M2	2138.3
32	3356	1.0	HOPS-359	0.4	141	29.0	J054722.90+002058.0	29.1	J054727.74+002035.8	49.4	1312	1.4	303	311.5	G205.46-14.56M2	2184.3
33	3344	0.3	HOPS-390	0.1	167	11.5	J054732.44+002021.7	0.2	J054736.60+002005.9	64.2	1338	1.5	303	204.0	G205.46-14.56M2	2215.5
34	3341	0.4	HOPS-364-B	0.1	167	74.5	J054736.57+002006.0	0.3	J054736.60+002005.9	0.7	1360	5.2	303	151.9	G205.46-14.56M2	2238.4

NOTE - Catalog entry name and separation distance to each of the protostellar catalogs studied to each of the ALMA detections. Maintaining the order presented in the current table the protostellar catalogs are the following: Megeath et al. (2012), Tobin et al. (2020), Spezzi et al. (2015), Gutermuth (in prep.), Marton et al. (2016), Könyves et al. (2020), Stutz et al. (2013), Dutta et al. (2020).

Chapter 4

Derived Properties

Table 4.1 lists the physical properties of each of the continuum sources, including the mass estimate, effective radius, and number density. The effective radius is computed from a geometric mean of the semi-major and semi-minor axes of the deconvolved size, and if the source is unresolved, the synthesized beam is used in place, and written as an upper limit.

4.1 Mass Estimates

Table 4.1: Physical Properties of ALMA Detections

Scr[a]	Mass[b] ($M_\odot$)	Radius[b] (au)	Number Density[b] (cm^{-3})
1	0.02	1010	7.6E+05
2	0.57	170	4.5E+09
3	1.89	130	3.2E+10
4	0.03	410	1.4E+07
5	0.06	620	8.7E+06
6	0.87	220	3.0E+09
7	0.39	110	9.3E+09
8	0.17	150	1.9E+09
9	0.05	680	5.9E+06
10	0.49	<290	>6.9E+08
11	0.13	90	6.3E+09
12	2.36	50	6.5E+11
13	0.57	120	1.0E+10
14	0.03	<290	>4.3E+07

to be continued on the next page

Table 4.1: (continued from previous page)

Scr[a]	Mass[b] ($M_\odot$)	Radius[b] (au)	Number Density[b] (cm^{-3})
15	3.96	110	1.2E+11
16	0.09	130	1.4E+09
17	0.03	<290	>4.2E+07
18	0.46	350	3.9E+08
19	0.97	200	4.1E+09
20	0.10	170	7.8E+08
21	0.06	<290	>8.4E+07
22	0.12	250	2.8E+08
23	0.07	960	2.7E+06
24	0.05	840	3.1E+06
25	0.32	170	2.4E+09
26	0.07	310	7.8E+07
27	0.20	140	2.6E+09
28	0.16	450	6.3E+07
29	0.30	180	1.7E+09
30	0.73	170	5.4E+09
31	0.12	170	8.3E+08
32	0.99	440	4.2E+08
33	0.34	150	3.2E+09
34	0.50	140	6.9E+09

[a] Running Index Number, the same as Table 3.1.

[b] Estimated mass, effective radius, and number density. Limit indicators for unresolved sources are shown. For these sources, the synthesized beam has been used in-place for the size; the effective radius should be taken as an upper limit, while the number density should be taken as a lower limit.

We estimate the mass of each continuum source using the standard equation:

$$M = 100\frac{d^2 S_\nu}{B_\nu(T_D)\kappa_\nu} \ , \tag{4.1}$$

where d is the distance, S_ν is the integrated flux at frequency ν, B_ν is the Planck function at the dust temperature of T_D, and κ_ν is the dust opacity. The factor of 100 represents the gas-to-dust ratio. We adopt a slightly updated value of distance, $d = 419$ pc, consistent with newer estimates from Zucker et al. (2019), and a core temperature of 20 K. At the

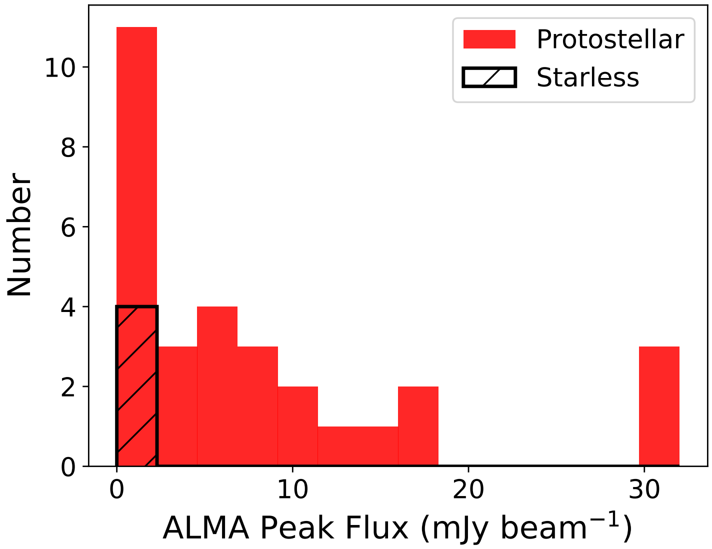

Figure 4.1: Distribution of ALMA detection peak fluxes. Detections with a peak flux greater than 30 mJy beam^{-1} are plotted in the final bin shown. We show both the protostellar ALMA detections in red (30 sources total), along with the candidate starless core detections in black (4 sources total).

submillimeter (and beyond), the relationship between opacity and wavelength is characterized by a power law ($\kappa \propto \lambda^{-\beta}$), with the index β representing the dust emissivity (Shirley et al., 2011). Many models show consistency with $\beta = 1.8$ at millimeter wavelengths (e.g. Sadavoy et al., 2013; Juvela et al., 2015; Chen et al., 2016). We extrapolate the Ossenkopf & Henning (1994) model to the given 106 GHz frequency of observation under the power law with $\beta = 1.8$, yielding our choice of $\kappa_\nu = 0.23$ cm^2 g^{-1}. Both temperature and the opacity were chosen based on NWT07 and Kirk et al. (2016), and the OH5 model extrapolation given directly above.

We calculate the mean density of each source as

$$n = \frac{3}{4\pi\mu m_{\rm H}} \frac{M}{R_{\rm eff}^3} \, , \tag{4.2}$$

where $\mu = 2.37$ is the mean molecular weight per free particle (Kauffmann et al., 2008) and $m_{\rm H}$ is the mass of a hydrogen atom. Both the computed mass and number density estimates are given in Table 4.1.

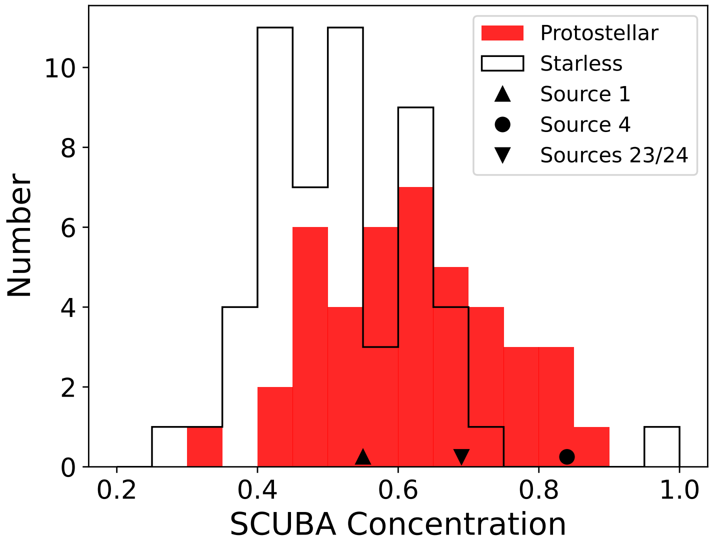

Figure 4.2: Distribution of core concentrations for dense cores in the Orion B North star forming region, computed from the re-classified NWT07 catalog (see Section 3.3 for details). The black line indicates cores classified as starless, while the red histogram indicates cores classified as protostellar in nature. We have excluded all values below a concentration of 0.2 (see Section 4.3 for discussion regarding this choice).

4.2 ALMA Peak Flux

Figure 4.1 shows the distribution of peak fluxes for both the protostellar and starless population of our ALMA detections. It is expected that the later stages of prestellar core evolution passes relatively quickly (Jessop & Ward-Thompson, 2000; Girichidis et al., 2014; Zamora-Avilés & Vázquez-Semadeni, 2014), in which the stage at which the prestellar core is detectable with ALMA. Compared to the development of a protostellar core, a starless core typically has a lower central density, and as a result, we should expect to see our prestellar cores have a low peak flux compared to the protostellar cores in our sample. All of our starless core detections notably lie in the lowest peak flux bin, suggesting that our observations agree with the overall picture of starless core evolution.

4.3 SCUBA Core Concentration

We measure the central concentration of dense cores from the NWT07 catalog, with the following definition:

$$C = 1 - \frac{1.13B^2F_{\rm tot}}{\pi R^2 F_{\rm pk}} \ , \tag{4.3}$$

where B is the beamsize, F_{tot} is the integrated flux, R is the effective radius, and F_{pk} is the peak flux (Johnstone et al., 2000).

The importance of self-gravity alongside the internal pressures of dense core structure, set the possible collapse of these structures into the smaller scales, usually associated with protostars. Bonnor-Ebert spheres (BE spheres) are a spherical, isothermal model for self-gravitating pressure-confined objects (Ebert, 1955; Bonnor, 1956), and this simple model predicts a range of values in terms of central concentrations. It is expected that dense cores become more centrally concentrated as they evolve in time, with uniform spheres having a central concentration value of 0.33 while the central concentration value of 0.72 is the maximum allowed for a stable BE sphere (Johnstone et al., 2000). Any cores above such a value do not have equilibrium solutions, and therefore must undergo gravitational collapse. Dense cores that are high in central concentration are usually found to be protostellar in nature (e.g., Johnstone et al., 2000; Kirk et al., 2006; Jørgensen et al., 2008).

Figure 4.2 shows the distribution of central concentration for all NWT07 cores in Orion B North. There are six starless dense cores that have concentrations lower than 0.33, the minimum value allowed for a uniform sphere. The NWT07 catalog for the Orion B North area, has a reported 1σ rms of 16 mJy beam^{-1}, and the analysis uses a detection threshold of $> 5\sigma$ relative to the local background for a robust source classification. Due to the lack of precision published in the values for the peak flux and the integrated flux (NWT07), for values of emission near the lowest reported limit of 0.1 Jy beam^{-1}, there exists a large amount of uncertainty. Since the central concentration uses both the measure of peak flux, as well as the total integrated flux, for the faintest cores, associated errors and uncertainties would propagate much more significantly. In this case, some reported values are found below the allowed minimum value of 0.33[1]. The surprisingly high concentration value of 0.955 associated with a starless core (the most elongated core reported in the NWT07 sample) similarly appears to be influenced by the same reasons as above. In all cases, the associated SCUBA-2 dense cores do have concentrations above the minimum 0.33 (Kirk et al., 2016) (see Appendix A.1 for discussion).

Our best starless core candidate, source 1 lies in a starless SCUBA dense core with a concentration value of 0.55. The remaining sources 4 and 23/24 lie in protostellar SCUBA dense cores with a central concentrations of 0.84 and 0.69 respectively. While there is a range of concentrations for both the starless and protostellar population of cores, as seen

---

[1] Additionally, for cores in close proximity to other cores in the catalog, NWT07 necessarily reduced the elliptical aperture size used to perform the 2D fit, to a level below the usually chosen 3σ contour. This choice partitions the extended emission between the cores, and could also contribute to the overall uncertainty in the measurements reported.

in Figure 4.2, more starless cores are found at lower concentrations, as expected for starless core populations in which they are more likely found in areas of extended emission still undergoing mass accretion and gravitational collapse.

In the analysis of the Ophiuchus molecular cloud, Jørgensen et al. (2008) found four starless cores with a high degree of central concentration, contrary to the previous study in the Perseus molecular cloud, where no starless cores were found to have a central concentration higher than 0.6 (Jørgensen et al., 2007). Kirk et al. (2017a) subsequently found no ALMA detections for SCUBA starless cores in Ophiuchus with concentrations below 0.6, but did detect all starless cores with higher concentrations than 0.6. Further evolved starless cores are expected to have a higher degree of central concentration as they near the time where collapse into a protostar will take place. All of our starless cores detections exhibit a high degree of central concentration, reinforcing this picture.

Chapter 5

Substructure and Fragmentation in Starless Cores

5.1 Numerical Simulations and Synthetic Observations

Turbulent simulations predict that fragmentation within dense cores begins during the starless core phase (Offner et al., 2012). Interferometers like ALMA are uniquely suited to detecting these small and faint density peaks within starless cores, while simultaneously filtering out larger-scale emission structures. In this section, we perform the same approach as Dunham et al. (2016) and Kirk et al. (2017a), and compute the number of starless core detections predicted by the turbulent fragmentation model for our observed Orion B North core sample.

We use magneto-hydrodynamic simulations of isolated, collapsing starless cores, with an initial core mass of 0.4 $M_{\odot}$, using the ORION Adaptive Mesh Refinement code base, to generate self-consistent, time-dependent physical conditions (Li et al., 2021). The simulation starts with a uniform density spherical core of gas, at a temperature of 10 K, with an initial number density of 1.6×10^5 cm^{-3}. The core is surrounded by a warm, low density medium, with a temperature of 1000 K, and a density 100 times lower than the initial core density. At the starting time step in the simulation, the gas velocities in the core are perturbed with a turbulent random field, and once set in motion, are allowed to decay with no additional energy injection (Offner et al., 2012). ORION evolves the calculations until shortly after the formation of a first hydrostatic core, input into the simulation as a sink particle. For more in-depth details on the descriptions of the simulations, we refer to the reader to Section 5.1.1 in Dunham et al. (2016).

To generate synthetic ALMA observations, we use the same turbulent simulation snapshots as in Dunham et al. (2016) and Kirk et al. (2017a). We take the total gas column density snapshots and convert them to total gas surface density, using the same mean molecular weight per free particle as in Equation 4.2. We then derive the mass in each pixel, and compute the flux map using Equation 4.1. Since the radiative effects are not directly calculated by the simulations, we take the additional step of computing the approximate temperature for every two-dimensional pixel. Similar to Dunham et al. (2016), we use an empirical relationship between the column density and the temperature, based on Bonnor-Ebert sphere models. This allows the temperature to be approximately characterized in a reasonable manner.

Finally, we create the synthetic observations using the appropriate antenna configurations, on-source time, and distance to Orion B North to match our current ALMA observations. The synthetic observations were generated using CASA's `simalma` task, and re-imaged with CASA's `tclean` task to mimic all imaging parameters used in the physical observations (see Section 2.2 for details). We choose the position of R.A. = 05:47:00 and Decl. = +00:05:00 for our simulated observations, which equates roughly to the center of our observational area in Orion B North. We use a total on-source time of 270 s, with 190 s at the more compact configuration, and 80 s at the more extended configuration, to match our real observations. We use integration times of 2 s at an effective mean frequency of 106 GHz with a bandwidth of 6 GHz, and include the default atmospheric noise model.

Figure 5.1 shows six time steps (from 0.151 Myr to 0.171 Myr) of the synthetic ALMA observations of the $0.4 M_\odot$ core simulation run.

5.2 Detecting Starless Cores

With the assumption of a continuous rate of star formation over the timescale at least as long as the core lifetimes, then similar to Dunham et al. (2016) and Kirk et al. (2017a), we can compute the expected number of detections as the following:

$$\text{Detections} > \frac{2}{3} \times N_{\text{total}} \times \left(\frac{n_{\text{Detectable}}}{n_{\text{Limit}}} \right)^{-0.5}, \tag{5.1}$$

where N_{total} is the number of starless cores observed, $n_{\text{Detectable}}$ is the core density at which our ALMA observations can detect the core, and n_{Limit} is the observed lower limit of the mean core densities as observed at single-dish resolution (in this case, the NWT07 data).

Figure 5.2 shows the distribution of core number densities for all cores in the Orion B North star forming region as presented in NWT07. The lowest density cores found in our population, near the left tail of the distribution (along with the one significant outlier) correspond to cores with atypical properties (highly elongated and very large cores), so we

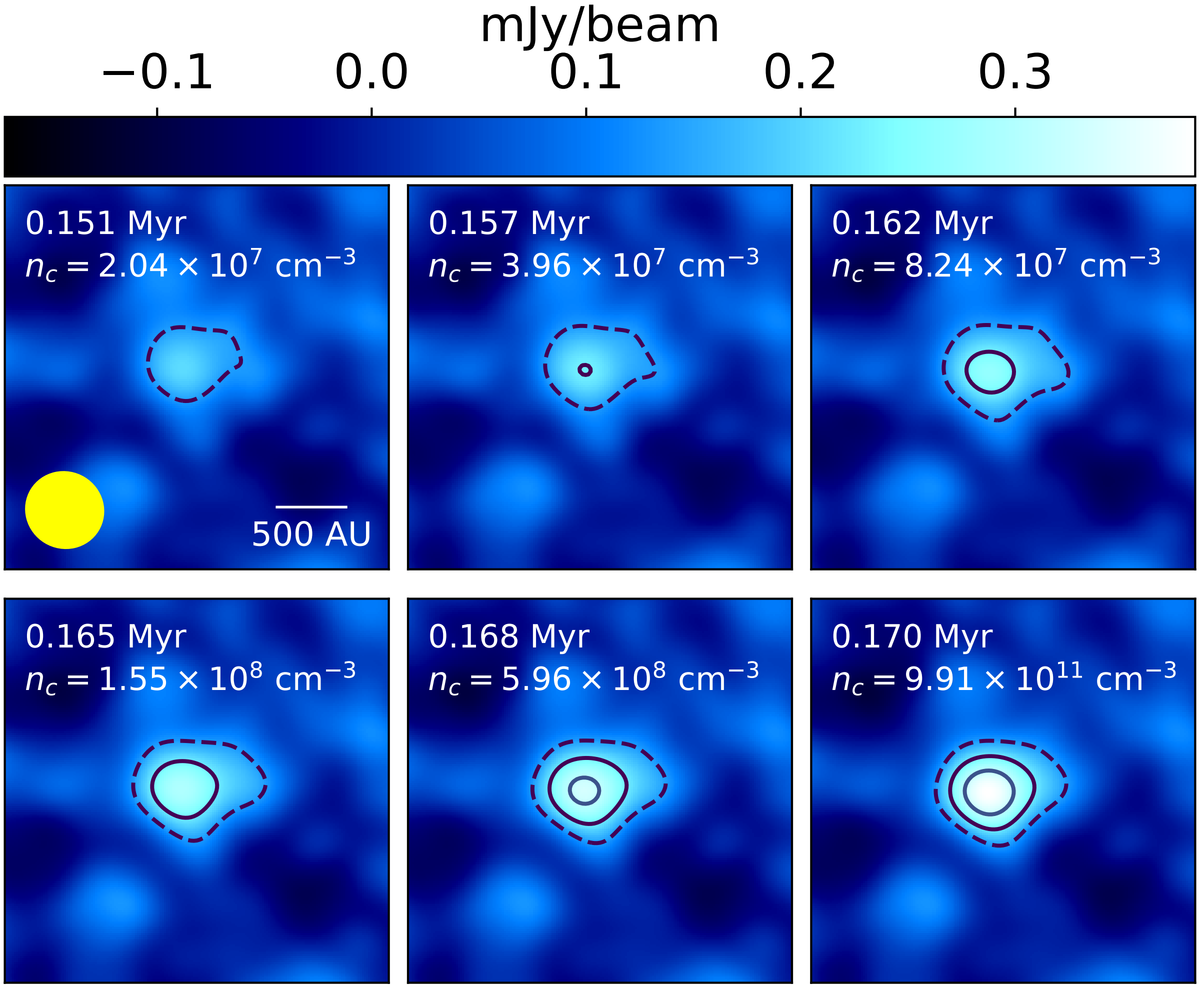

Figure 5.1: Synthetic ALMA 106 GHz observations of the $0.4 M_\odot$ simulation, at six given timesteps, indicated in each panel along side the central density of the core. The synthesized beam is given in the first panel as a yellow ellipse in the bottom left corner. The dashed contour represents the 3σ level. The solid contours start at a level of 5σ and increase by 2σ, where $1\sigma \sim 0.045$ mJy beam^{-1}. We consider a robust detection to be a minimum of 5σ.

briefly explain our choice for the observed lower limit chosen for our calculations[1]. We compute the number density of a dense core whose size is equal to the beamsize ($14''$) and which lies at the sensitivity limit of the NWT07 dataset, to represent an object at the minimum detectable density. NWT07 classifies any object at 5σ above the local noise level as a positive detection, and for the Orion B North area, the 1σ rms noise is given as 16 mJy beam^{-1}. This produces a minimum detectable density of 2.11×10^4 cm^{-3}. For comparison, our lowest density starless core observed has an estimated density of 5.68×10^3 cm^{-3}, although as can be seen in Figure 5.2, only a small number of the starless cores have estimated densities below 2.11×10^4 cm^{-3}. Our derived value of 2.11×10^4 cm^{-3} agrees well with the lower tail of the distribution as shown in Figure 5.2, and is representative of a typical core seen in our observations.

A newer and more sensitive sub-millimetre study of Orion B North dense cores, performed with SCUBA-2 (Kirk et al., 2016), showed dense core densities to be in the range of $1 - 100 \times 10^4$ cm^{-3}. Additionally, protostellar cores tend to have slightly higher number densities on average, compared to the starless cores (Kirk et al., 2016). The SCUBA core densities, as shown in Figure 5.2, show a similar range of densities with the same slight increase of the protostellar population (see Appendix A.1 for discussion on basic differences between SCUBA and SCUBA-2 datasets). Our above choice of minimum detectable density of 2.11×10^4 cm^{-3} agrees well in both the context of the SCUBA derived core densities, as well as the study using SCUBA-2 from Kirk et al. (2016).

The central core peak in the simulations is only detected at a 5σ level after 0.157 Myr, when the central core density reaches 3.96×10^7 cm^{-3}. We use this as the criteria for a robust detection, and we set the detectability limit as such.

In total, for the Orion B North region studied, we have $N_{\text{total}} = 58$ starless cores (as re-classified in Section 3.3), with a minimum density of $n_{\text{Limit}} = 2.11 \times 10^4$ cm^{-3}, along with the detectability limit of our ALMA configuration $n_{\text{Detectable}} = 3.96 \times 10^7$ cm^{-3}. Using Equation 5.1 we predict a minimum of one (0.893) starless core that has enough substructure for a positive detection in our observations.

Our lowest estimated core density (5.68×10^3 cm^{-3}) belongs to the same highly elongated core, as mentioned earlier in this section, thus if we instead utilized the second lowest estimated core density (1.36×10^4 cm^{-3}) in place of our chosen detectability limit (a more appropriate lowest density estimate), we would lower our expected number of starless core detections to 0.72. The results would remain unaffected with this difference in chosen de-

---

[1] The most atypical core, BN-547034+1950, is the same extremely high concentration core as detailed in Section 4.3.

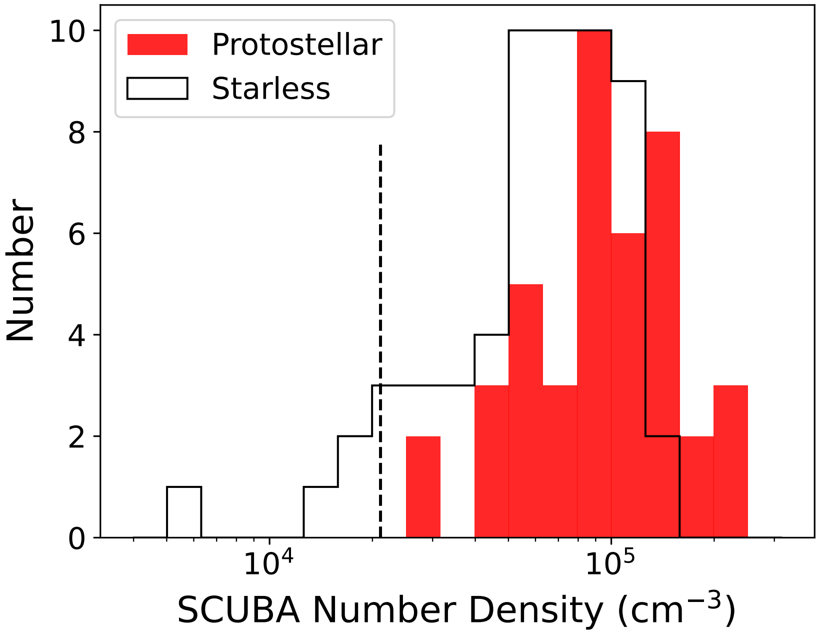

Figure 5.2: Distribution of NWT07 core number densities. The black histogram indicates cores classified as starless, while the red filled histogram indicates cores classified as protostellar in nature. The vertical black dashed line indicates the minimum detectable density, as computed in Section 5.2.

tectability limit.

In our observed sample, we have 4 starless core candidates, however, only one is found in the central portion of the primary beam, suggesting that the starless core detection was most likely the intended core to be studied, consistent with the model predictions.

Due to the non-detections in the Chameleon I study, Dunham et al. (2016) proposes specific implications for the starless core population based on the predictions from the synthetic observations. One such implication is based on the assumption of continuous star formation, which is typically assumed for small population studies, as is done in this study. This assumption has been previously tested in a variety of ways, over different dense core populations (e.g., Pattle et al., 2015; Tsitali et al., 2015). For instance, Belloche et al. (2011) shows the relationship between the mass and the size of dense cores (also shown for the same population in Dunham et al., 2016), where we can compare the region taken up by the dense cores, against the areas showing instability for Bonnor-Ebert sphere models. If most of the starless cores in a region are stable and not currently collapsing, they can be shown to disagree with a constant rate of star formation (Dunham et al., 2016). In the same context, the low ratio of Class 0+I to Class II YSOs in Chamaeleon I as presented in Dunham et al.

(2015), indicates a decelerating rate of star formation, which also lends weight to the lack of starless core substructure detections in Dunham et al. (2016).

As introduced in Section 1, a BE sphere-like model has a smooth and broad density profile, as driven by completely thermal evolution processes. Observations taken with an interferometer leads to filtering effects, which depending on the scale of emission, can impact the detectability of such objects. Dunham et al. (2016) demonstrated that structures generated from turbulent fragmentation should be detectable at a rate approximately 100 times higher than the BE sphere-like model for their ALMA observational setup of Chamaeleon I. Since our ALMA observations are very similar to those taken in both the Chamaeleon I ALMA study (Dunham et al., 2016) and the Ophiuchus ALMA study (Kirk et al., 2017a), we should also expect to see a lack of detections if the evolution and resulting density structure is similar to that of a BE sphere-like model.

A single detection under the turbulent fragmentation model is not a large number for model testing, however, we note that under the BE sphere-like model, it would be very unlikely to get a single detection. With the combination of Orion B North and Ophiuchus (Kirk et al., 2017a), we now have two studies which show that the fragmentation model serves to represent a clearer picture of the on-going evolution of starless core evolution.

Chapter 6

Comparison to Chamaeleon I and Ophiuchus

Through the analysis of the Chamaeleon I star forming region, Dunham et al. (2016) expected two starless core detections under the turbulent fragmentation model, but found no such detections in their observations. Dunham et al. (2016) proposed three arguments as to why no starless core detections were found in the Chamaeleon I cloud: the lack of continuous star formation in the cloud, that the assumption of the core lifetime proportionality to the free fall time is not correct, or that the numerical simulations are not applicable. This is in direct contrast to the study performed by Kirk et al. (2017a), where the dense core population of the Ophiuchus star forming region was analyzed, and found to agree with those same fragmentation models with two tentative detections compared with two predicted.

With the addition of the Orion B North observations, we are now in a position to search for differences in the core populations per cloud as a possible explanation for the lack of detections in Chamaeleon I. A basic virial analysis performed by Tsitali et al. (2015) studied the core's self-gravity contribution in comparison with the thermal and non-thermal pressure support within the dense core population in the Chamaeleon I/III clouds, showing that the cores are gravitationally unbound, suggesting that star formation may not continue.

A full virial analysis allows for more information regarding specific physical processes that may be guiding differences in star forming regions. Some additional virial terms are pressure support from cloud-wide turbulence, pressure support from the molecular cloud weight, and contributions from magnetic fields (e.g., Pattle et al., 2015; Kirk et al., 2017b; Kerr et al., 2019).

We run both the simple Jeans analysis and a fuller virial analysis including the larger-scale external pressure binding terms, to provide context as to why there is such a difference in the predicted number of detections between the star forming clouds studied. Since our goal is to compare the core populations between clouds, we adopt comparable datasets for all three clouds; unfortunately no such uniform data was available for the magnetic field strength, so we exclude this term. We follow with descriptions of the adopted comparable datasets as they pertain to both the Jeans analysis and the fuller virial analysis.

6.1 Datasets Used

6.1.1 Dust Continuum-based Properties - Mass and Size

We adopt the dataset from Belloche et al. (2011) for the Chamaeleon I cloud, Jørgensen et al. (2008) for Ophiuchus, and NWT07 for Orion B North, which are sub-millimetre dust continuum observations from single dish telescopes deriving the mass and size of the dense core population.

Chamaeleon I observations were conducted with the LABOCA bolometer array on the APEX telescope, measuring the dust continuum at 870μm (Belloche et al., 2011). Cores were identified using `Gaussclumps` (Stutzki & Guesten, 1990; Kramer et al., 1998), on the continuum maps of Chamaeleon I produced by Motte et al. (1998, 2007).

Both the Ophiuchus and Orion B North datasets were observed with the SCUBA instrument on the JCMT at a wavelength of 850μm (Nutter & Ward-Thompson, 2007; Jørgensen et al., 2008). In the case of Ophiuchus, the core finding algorithm `clumpfind` was utilized (Williams et al., 1994) and the core sizes were estimated based on the number of pixels contained within the `clumpfind` core boundary. For Orion B North, NWT07 estimated the core sizes, in most cases, by placing an elliptical aperture on each source and approximately matched to the position of the 3σ contour.

The assignment of emission to one source compared with another, among other decisions made with certain core finding algorithms, can strongly affect the derived core properties specifically in crowded regions, including both the radius measurement and resulting mass estimate (Pineda et al., 2009). For instance, `Gaussclumps` decompose the observed intensity distribution into the emission of individual, Gaussian shaped clumps by iteratively subtracting fitted clumps. Meanwhile, `clumpfind` analyzes clumpy structure by contouring the data at a multiples of the rms noise, then searches for distinct peaks of emission and associates surrounding lower-intensity emission with each. Biases exist for any chosen core finding algorithms, and some may outperform others in certain cases (Pineda et al., 2023). Ideally, a population-to-population virial analysis would use the same core finding algorithm in order to keep any bias consistent across the sample. Nonetheless, we directly adopt the masses and sizes as reported in the aforementioned papers for our analysis.

6.1.2 Dense Gas Kinematics

NH_3 and similar other N-bearing species are often found to be a good tracer of dense core material and can usually probe deeper layers than similar measurements conducted with C-bearing species (e.g., Jijina et al., 1999; di Francesco et al., 2007). These measurements provide similar measures of kinematic core properties across different star forming environments (Johnstone et al., 2010). The Green Bank Ammonia Survey (GAS, Friesen et al., 2017) mapped $NH_3(1,1)$ and $NH_3(2,2)$ in the Orion B North and Ophiuchus clouds, providing measurements of the dense gas excitation temperature and thermal and non-thermal components of the line width.

Tsitali et al. (2015) observed many different spectral lines in the Chamaeleon I cores; we adopt the $N_2H^+(1-0)$ data as being the most comparable to the NH_3 data available for the other two clouds. In the study of dense gas tracers in Perseus, Johnstone et al. (2010) show that the kinematic properties of NH_3 and N_2H^+ are extremely similar, showing that these species are well coupled, regardless of the physical conditions in the dense core gas. This reinforces our choice to only use the $N_2H^+(1-0)$ for the Chamaeleon I region. We assume a dense core gas temperature of $T = 10$ K to derive the non-thermal velocity dispersions, the same as Tsitali et al. (2015).

6.1.3 Larger Scale Turbulent Material

The turbulent motions present in the lower density material surrounding the dense cores is often traced by various CO isotopologues. The all-sky CO surveys[1] using the CfA and Cerro Tololo telescopes provides the best source of comparable CO data across all three regions studied (Dame et al., 2001; Dame & Thaddeus, 2022). We choose to utilize the newer Northern Sky Survey of Dame & Thaddeus (2022), which is a large extension of the Galactic plane CO survey of Dame et al. (2001) to the entire northern sky ($\delta > -17°$). This survey uniformly samples the high-latitude sky with a resolution of 0.25 degrees, along with spectra with uniform sensitivity of 0.18 K in 0.65 km s^{-1} channels across a velocity range of ± 47.1 km s^{-1}. Due to the relatively poor spectral resolution, we expect these contributions to lead to an overestimate of the associated linewidth; we discuss the implications in Section 6.4.

---

[1] `https://lweb.cfa.harvard.edu/rtdc/CO/`

6.1.4 Cloud Weight

Finally, we utilize the all-sky dust extinction maps of Rowles & Froebrich (2009) to estimate the compression on the dense cores due to the weight of their surrounding molecular cloud. We use the $N = 25$ star maps to maximize the angular resolution available (see Section 2.1 in Rowles & Froebrich, 2009).

6.2 Data Coverage

The chosen extinction and ^{12}CO maps are all-sky, therefore and have uniform coverage over all three clouds studied. The dense gas tracers, NH_3 and N_2H^+, are more limited in terms of area mapped and area detected. We briefly explain the kinematic dataset coverage with respect to each dense core population studied.

6.2.1 Ophiuchus

GAS provides measurements of the dense gas line width and temperature, however, the latter quantity covers a smaller area as the fainter $NH_3(2, 2)$ line needs to be detected *in addition* to the $NH_3(1, 1)$ transition. In order to maximize the kinematic data available, we assume a temperature of $T = 13$ K for all cores that have only line width information available (taken as the mean temperature for all dense cores covered by GAS, in Ophiuchus). In Ophiuchus, 55 of the 66 dense cores, or 83% have GAS line width measurements, with a subset of 29 cores containing kinetic temperature measurements. This dataset represents the largest overlap with the GAS kinematic data in our three cloud comparison.

Virial analyses of Ophiuchus based on SCUBA-2 data, have recently been published (Pattle et al., 2015; Kerr et al., 2019), however, for consistency with the SCUBA-based core catalogue used for the ALMA survey, we run our own independent analysis.

6.2.2 Orion B North

In Orion B North, only 18 of the 73 dense cores, or 25% have GAS line width measurements, with a subset of 16 cores containing kinetic temperature measurements. The GAS mapping of Orion B North appears incomplete, resulting in a low amount of coverage in comparison with Ophiuchus. We note that the 16 cores with kinematic information available for this analysis are representative of the overall dense core population in Orion B North. We assume a temperature of $T = 15$ K for all cores which only have line width measurements (again, taken as the mean temperature for all dense cores covered by GAS, in Orion B North).

6.2.3 Chamaeleon I

In Chamaeleon I, 19 of the 60 dense cores, or 33%, are detected in the $N_2H^+(1-0)$ line (Tsitali et al., 2015). Tsitali et al. (2015) do detect many more of the cores in lower density gas tracers, however, as noted in Section 6.1.2, we adopt only the $N_2H^+(1-0)$ data, as being the most comparable to the data available in the other two regions.

In total, we present the 19 dense cores in the Chamaeleon I, 55 dense cores in the Ophiuchus star forming region, and 18 dense cores in the Orion B North region, for a total of 92 dense cores our virial analysis. We utilize the protostellar re-classification conducted by Dunham et al. (2016) for Chamaeleon I, Kirk et al. (2017a) for Ophiuchus, and this work for Orion B North (see Table 2.1 and Section 3.3) to separate the dense core populations into starless cores and protostellar cores as needed for the analysis.

6.3 Jeans Analysis

We first compute the virial parameter, α, which indicates the relative contribution of self-gravity versus that of thermal and non-thermal support. It is computed for a uniform, ellipsoid source, following the standard method outlined in Bertoldi & McKee (1992):

$$\alpha = \frac{5\sigma_{\rm tot}^2 R}{GM} \ , \tag{6.1}$$

where R is the core radius, G is the gravitational constant, and M is the core mass. The total velocity dispersion, $\sigma_{\rm tot}$, is given by the following:

$$\sigma_{\rm tot} = \sqrt{(\sigma_{\rm obs}^2 - \sigma_{\rm th,mol}^2 + \sigma_{\rm th,mean}^2)} \ , \tag{6.2}$$

with $\sigma_{\rm obs}$ representing the observed dense gas line width. The mean and molecular velocity dispersions are calculated as follows:

$$\sigma_{\rm th,mean} = \sqrt{\frac{k_B T}{\mu m_H}} \ , \tag{6.3}$$

$$\sigma_{\rm th,mol} = \sqrt{\frac{k_B T}{m_{\rm mol}}} \ , \tag{6.4}$$

where the molecular weight of the mean particle is μm_H ($\mu = 2.37$), and $m_{\rm mol} = \mu_{\rm mol} m_H$ is the molecular mass of the tracer, in this case NH_3. As highlighted in Section 6.1.2, we compute these values for the Orion B North and Ophiuchus regions from the GAS data.

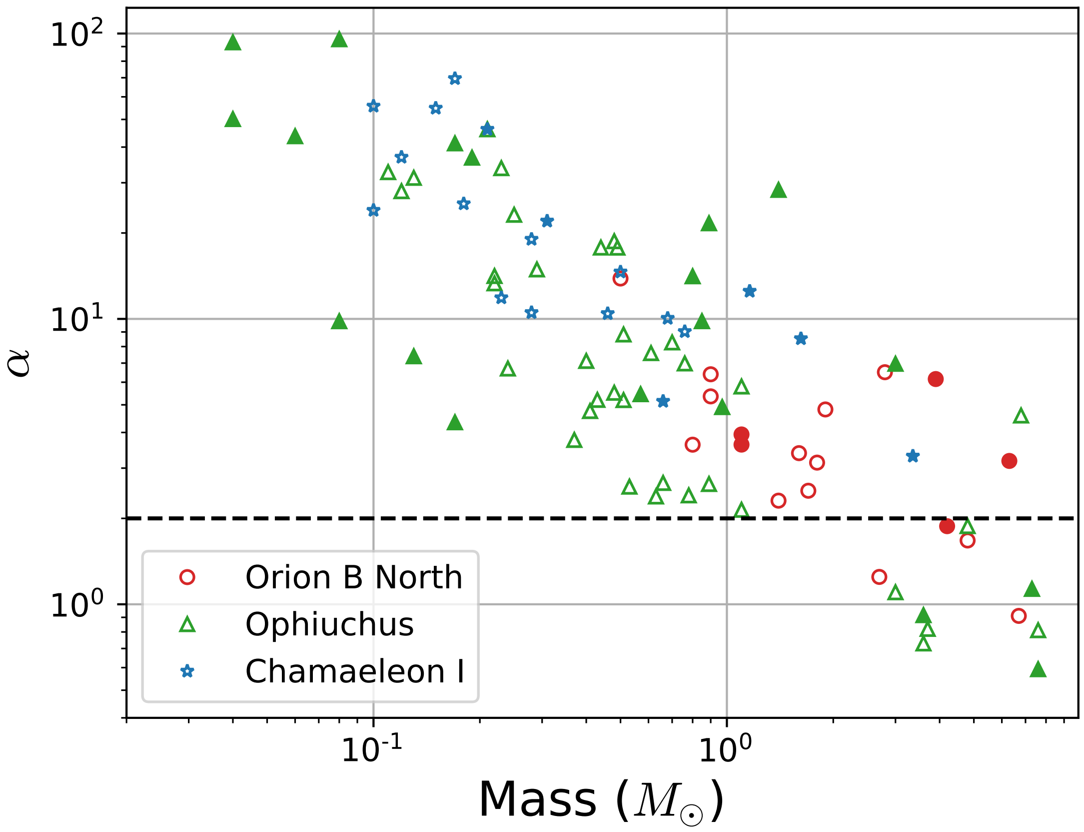

Figure 6.1: Virial parameter versus core mass, computed for each of the three cloud dense core populations. Each color represents a distinct star forming region. Open markers show the *starless* core population, while filled markers show cores that are protostellar in nature. Cores lying above the dashed line are considered gravitationally unbound.

We use the fitted line width and temperature values for the pixel that the core's peak lies within, where available. We utilize the published values by Tsitali et al. (2015) for their pointed observations of the Chamaeleon I cores from Belloche et al. (2011) and assume the same temperature of $T = 10$ K, as outlined in Section 6.1.2.

Figure 6.1 plots the virial parameter against the core mass for all three core populations. None of the Chamaeleon I starless cores fall below the dashed line, indicating that all cores are gravitationally unbounded under this simple virial analysis. In contrast, 15% (8/55) and 22% (4/18) dense cores have $\alpha \leq 2$ in Ophiuchus and Orion B North respectively. Many of the aforementioned cores that are found to be bounded are also starless in nature.

In Ophiuchus, Kerr et al. (2019) found that the majority of dense cores were found to be unbounded when only considering self-gravity and thermal and non-thermal motions. Kerr et al. (2019) found only 7% of such cores (5/74) had $\alpha \leq 2$ in the Ophiuchus region, presenting a lower percentage of cores compared to this study's 15%. Due to the different dust-based core catalogs used for the analysis, identical results are not expected.

In summary, in light of characteristically different results between the Chamaeleon I cloud and the others clouds in this study, we conduct a broader look at further physical mechanisms through additional virial terms.

6.4 Virial Analysis

A number of recent studies implement a more complete virial analysis, often case in terms of energy densities, to gain a fuller picture of the core boundedness (e.g., Pattle et al., 2015; Kirk et al., 2017b; Keown et al., 2017; Kerr et al., 2019). Similar to previous studies, we incorporate both the external pressure contributions from the weight of the surrounding molecular cloud, as well as the pressure from the surrounding turbulent medium, but lack uniform data for the contributions of magnetic fields (as introduced in Section 6).

Following the method outlined in Pattle et al. (2015), we describe the contributions given by internal motions and self-gravity in the core, as well as the external pressure contributions from the surrounding cloud as the following:

$$\Omega_{\mathrm{k}} = \frac{3}{2} M \sigma_{\mathrm{tot}}^2 \ , \tag{6.5}$$

$$\Omega_{\mathrm{g}} = -\frac{3}{5} \frac{GM^2}{R} \ , \tag{6.6}$$

$$\Omega_{\mathrm{P}} = -4\pi P R^3 \ . \tag{6.7}$$

We follow Kerr et al. (2019) and choose a constant factor of $-3/5$ for Equation 6.6, appropriate for sources with constant density, which is a better approximation for cores following the typical $\rho \propto r^{-1}$ density profile.

The contribution of the molecular cloud weight is computed with the following (McKee, 1989; Kirk et al., 2017b):

$$P_{\mathrm{w}} = \pi G \Sigma \bar{\Sigma} \ , \tag{6.8}$$

where Σ is the surface mass density along the line-of-sight of the dense core, and $\bar{\Sigma}$ is the mean mass surface density across the entire cloud. This formulation assumes that the large scale structure is spherically symmetric, with a density falloff following $\rho \propto r^{-1}$; the effect of different geometries is discussed in Kirk et al. (2017b). We compute the mean mass surface density using all pixels above $A_{\mathrm{v}} = 3$ mag associated with the cloud in our chosen datasets. We convert the extinction into H_2 column density using a conversion of 1 mag $= 9.4 \times 10^{20}$ cm^{-2} from Bohlin et al. (1978). The mean extinctions are similar across all three clouds, with values of 4.91 mag, 5.23 mag, 4.95 mag, for Orion B North, Ophiuchus, and Chamaeleon I clouds respectively. Due to the use of comparatively lower resolution data, the contribution of core material to the extinction measurement is minimal, and further processing of the extinction maps are not required.

To incorporate the contribution from large-scale turbulent pressure, we calculate the line widths of the all-sky CO data (see Section 6.1.3) at the position of each core. We utilize a single component Gaussian model, which is a reasonable representation based on visual checks of the spectra. As is typical for virial analyses, we make the assumption that turbulence acts as an isotropic pressure support, computed with the following expression:

$$P_{\mathrm{t}} = n_{\mathrm{CO}} \mu_{\mathrm{mn}} m_{\mathrm{H}} \sigma^2_{\mathrm{tot,CO}} \ , \tag{6.9}$$

where the density of the gas that the ^{12}CO lines are probing is given by n_{CO}, and the fitted linewidth is given by $\sigma_{\mathrm{tot,CO}}$. Due to the lower resolution of the ^{12}CO data (0.25 degrees), we utilize the mean density found in star forming cloud environments, 250 cm^{-3} (Bergin & Tafalla, 2007) to represent the density of the gas that the ^{12}CO data is probing.

Our virial results are presented in Table 6.1, for the total 92 dense cores across the three star forming regions. A dense core is defined as being in a state of virial equilibrium when $2\Omega_{\mathrm{k}} = -(\Omega_{\mathrm{g}} + \Omega_{\mathrm{P,t}} + \Omega_{\mathrm{P,w}})$. If the virial ratio (as given in the final column of Table 6.1) is greater than one, a core will be bounded, while a ratio less than one indicates that the core is unbounded and most likely will disperse over time. Figure 6.2 shows the confinement ratio on the vertical axis, describing the relative contributions of both external pressure and self-gravity, as a function of the virial ratio.

The addition of the contributions of the external pressure terms, do generally shift more cores into the bound regime, as compared to our results from the simple Jeans analysis. The relative contribution of external pressure indicates that the cloud weight pressure is responsible for much more of the binding in Chamaeleon I cores, up to an order of magnitude on average compared with those found in the Ophiuchus region. Similar to Tsitali et al. (2015), we find Cha1-C1 (also known as Cha-MMS1) to be gravitationally dominated, the only core in our analysis in this domain. Cha-MMS1 is a first hydrostatic core candidate (Belloche et al., 2006, 2011; Tsitali et al., 2013), explaining the much larger contribution of

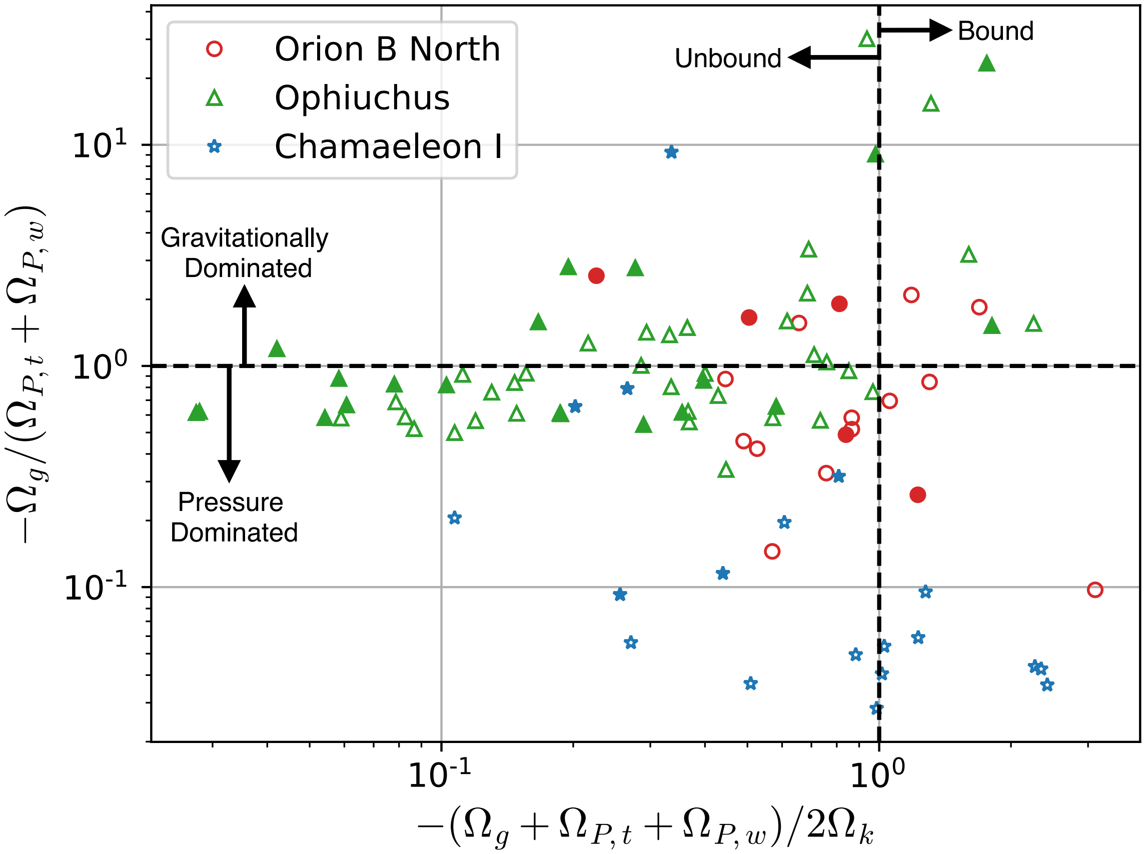

Figure 6.2: Confinement ratio versus the virial ratio, as computed for each of the three cloud dense core populations. See Figure 6.1 for plotting conventions. Cores lying above the horizontal dashed line are considered gravitationally dominated, while cores under the dashed line are considered pressure dominated. Cores lying to the right hand side of the vertical dashed line are bounded given the full virial equation used for this study.

the gravitational virial term in comparison its external pressure term.

With the addition of turbulent and cloud weight pressures, 54% (7/13) of *starless* cores in Chamaeleon I, 8% (3/36) of *starless* cores in Ophiuchus, and 38% (5/13) of *starless* cores in Orion B North qualify as bound. Compared to the results from Kerr et al. (2019), in which 36% of the starless cores were found to become bound in the full virial analysis, we find a lower amount of starless cores in Ophiuchus that are classified as bound. Nonetheless, most cores in Ophiuchus have more equal contributions from the two pressure sources, similar to the results from Kerr et al. (2019).

The all-sky CO survey datasets used in this analysis were chosen for their comparable observations and spectral resolutions across the entire northern sky (see Section 6.1.3). The individual all-sky CO survey datasets for Chamaeleon (Boulanger et al., 1998), Ophiuchus (de Geus et al., 1990), and Orion (Wilson et al., 2005) do give a higher angular resolution for the Orion and Chamaeleon regions (0.125 degrees), and a higher spectral resolution for Ophiuchus (0.26 km s^{-1}). Utilizing these individual surveys in-place of our chosen CO dataset yielded an increase in the fitted linewidths of approximately 20% on average, and no more than 30% in difference. Due to the marginal increase in resolution of the individual surveys compared to the all-sky survey, the final derived values along with our conclusions, do not significantly change the results shown. Due to the coarse spectral resolution of the all-sky survey used (similarly for the unused individual surveys), we are likely to have overestimated our turbulent pressures across all three core populations.

Table 6.1: Starless Core Virial Properties

Core Name[a]	Mass[a] ($M_\odot$)	R_{eff}[a] (pc)	T_{k}[b] (K)	σ_{obs}[b] (km s^{-1})	Ω_{k}[c] (erg)	$-\Omega_{\mathrm{g}}$[c] (erg)	$-\Omega_{\mathrm{P,w}}$[c] (erg)	$-\Omega_{\mathrm{P,t}}$[c] (erg)	Virial[d] Ratio
Orion B North									
BN-546074-01342	6.30	0.068	17.1	0.449	4.75e+43	2.99e+43	3.57e+42	1.45e+43	5.04e-01
BN-546097-00552	0.50	0.035	15.0	0.353	2.53e+42	3.65e+41	5.42e+41	1.98e+42	5.70e-01
BN-546135-00525	1.10	0.045	12.8	0.213	2.75e+42	1.40e+42	1.32e+42	4.02e+42	1.23e+00
BN-546310-00234	4.20	0.053	16.1	0.284	1.61e+43	1.72e+43	2.34e+42	6.66e+42	8.11e-01
BN-546433-00148	0.80	0.049	12.3	0.119	1.22e+42	6.72e+41	1.31e+42	5.61e+42	3.11e+00
BN-546280-00145	1.90	0.043	13.7	0.379	1.05e+43	4.34e+42	1.44e+42	3.54e+42	4.45e-01
BN-546276-00057	3.90	0.047	15.5	0.630	5.16e+43	1.68e+43	1.96e+42	4.60e+42	2.26e-01
BN-546321-00044	0.90	0.035	12.8	0.320	3.78e+42	1.18e+42	8.10e+41	1.99e+42	5.26e-01
BN-546532-00018	4.80	0.070	16.7	0.221	1.41e+43	1.69e+43	3.42e+42	1.65e+43	1.30e+00
BN-546334-00006	1.10	0.038	15.4	0.210	2.95e+42	1.63e+42	8.09e+41	2.52e+42	8.40e-01
BN-546244-00001	2.80	0.059	15.0	0.470	2.22e+43	6.83e+42	3.87e+42	1.11e+43	4.90e-01
BN-546450+00021	1.70	0.036	16.0	0.234	5.22e+42	4.17e+42	5.08e+41	2.16e+42	6.56e-01
BN-546350+00029	1.60	0.044	17.0	0.235	5.06e+42	2.99e+42	1.17e+42	4.61e+42	8.66e-01
BN-546405+00032	2.70	0.042	15.4	0.153	5.60e+42	8.99e+42	8.17e+41	3.47e+42	1.18e+00
BN-546267+00101	1.80	0.045	13.6	0.259	5.77e+42	3.68e+42	1.32e+42	5.00e+42	8.65e-01
BN-546275+00135	1.40	0.038	13.1	0.183	3.04e+42	2.64e+42	7.93e+41	3.00e+42	1.06e+00
BN-546499+00204	6.70	0.068	17.7	0.155	1.54e+43	3.38e+43	3.05e+42	1.53e+43	1.69e+00
BN-546362+00550	0.90	0.035	15.0	0.270	3.16e+42	1.18e+42	7.36e+41	2.87e+42	7.57e-01
Ophiuchus									
162608-24202	0.76	0.028	13.0	0.355	3.74e+42	1.07e+42	5.25e+41	5.42e+41	2.86e-01
162610-24195	0.48	0.023	13.0	0.551	4.91e+42	5.24e+41	2.78e+41	2.94e+41	1.12e-01

to be continued on the next page

Table 6.1: (continued from previous page)

Core Name[a]	Mass[a] ($M_\odot$)	$R_{\rm eff}$[a] (pc)	$T_{\rm k}$[b] (K)	$\sigma_{\rm obs}$[b] (km s^{-1})	$\Omega_{\rm k}$[c] (erg)	$-\Omega_{\rm g}$[c] (erg)	$-\Omega_{\rm P,w}$[c] (erg)	$-\Omega_{\rm P,t}$[c] (erg)	Virial[d] Ratio
162610-24231	0.44	0.023	13.0	0.509	3.92e+42	4.41e+41	2.85e+41	2.94e+41	1.30e-01
162610-24206	0.80	0.032	13.0	0.514	7.24e+42	1.03e+42	8.34e+41	8.42e+41	1.87e-01
162614-24232	0.13	0.012	13.0	0.493	1.09e+42	7.01e+40	5.35e+40	4.85e+40	7.87e-02
162614-24234	0.25	0.018	13.0	0.485	2.04e+42	1.76e+41	1.58e+41	1.54e+41	1.20e-01
162614-24250	1.40	0.039	13.0	0.920	3.69e+43	2.61e+42	1.69e+42	1.47e+42	7.80e-02
162615-24231	0.49	0.025	13.0	0.514	4.43e+42	4.98e+41	4.28e+41	3.88e+41	1.49e-01
162616-24235	0.23	0.017	13.0	0.586	2.62e+42	1.56e+41	1.62e+41	1.37e+41	8.66e-02
162617-24235	0.89	0.031	13.0	0.709	1.44e+43	1.33e+42	8.92e+41	7.32e+41	1.03e-01
162622-24225	3.00	0.042	13.0	0.622	3.81e+43	1.09e+43	1.98e+42	1.93e+42	1.95e-01
162624-24162	0.06	0.007	13.0	0.520	5.54e+41	2.54e+40	8.21e+39	1.30e+40	4.21e-02
162626-24243	7.30	0.048	18.3	0.305	3.22e+43	5.70e+43	3.44e+42	2.84e+42	9.81e-01
162627-24233	3.00	0.023	18.3	0.259	1.09e+43	1.98e+43	3.34e+41	3.24e+41	9.38e-01
162628-24235	7.60	0.043	18.5	0.261	2.80e+43	6.91e+43	2.46e+42	2.03e+42	1.31e+00
162628-24225	4.80	0.051	18.1	0.313	2.18e+43	2.32e+43	3.50e+42	3.39e+42	6.90e-01
162633-24261	6.80	0.073	13.0	0.574	7.48e+43	3.26e+43	1.23e+43	9.65e+42	3.64e-01
162641-24272	0.85	0.033	13.0	0.425	5.56e+42	1.13e+42	1.21e+42	8.79e+41	2.90e-01
162644-24173	0.22	0.015	13.0	0.367	1.14e+42	1.71e+41	7.99e+40	1.04e+41	1.56e-01
162644-24345	0.04	0.007	13.0	0.445	2.83e+41	1.13e+40	9.72e+39	9.65e+39	5.42e-02
162644-24253	0.41	0.023	14.8	0.173	9.09e+41	3.83e+41	3.69e+41	2.87e+41	5.71e-01
162646-24242	0.40	0.022	13.0	0.271	1.34e+42	3.76e+41	3.44e+41	2.60e+41	3.66e-01
162648-24236	0.51	0.026	13.0	0.330	2.25e+42	5.10e+41	5.95e+41	9.04e+41	4.47e-01
162660-24343	3.60	0.053	10.3	0.109	4.57e+42	1.25e+43	4.30e+42	3.75e+42	2.25e+00
162705-24363	0.08	0.010	13.0	0.779	1.54e+42	3.23e+40	2.60e+40	2.65e+40	2.75e-02

to be continued on the next page

Table 6.1: (continued from previous page)

Core Name[a]	Mass[a] ($M_\odot$)	$R_{\rm eff}$[a] (pc)	$T_{\rm k}$[b] (K)	$\sigma_{\rm obs}$[b] (km s^{-1})	$\Omega_{\rm k}$[c] (erg)	$-\Omega_{\rm g}$[c] (erg)	$-\Omega_{\rm P,w}$[c] (erg)	$-\Omega_{\rm P,t}$[c] (erg)	Virial[d] Ratio
162705-24391	0.53	0.023	11.4	0.128	8.00e+41	6.19e+41	2.79e+41	3.16e+41	7.59e-01
162707-24381	0.04	0.007	13.0	0.634	5.26e+41	1.13e+40	8.51e+39	9.65e+39	2.80e-02
162709-24372	0.19	0.015	13.0	0.611	2.34e+42	1.27e+41	6.80e+40	7.72e+40	5.83e-02
162711-24393	0.21	0.017	13.0	0.678	3.12e+42	1.35e+41	1.15e+41	1.18e+41	5.90e-02
162712-24290	0.11	0.012	15.2	0.469	8.72e+41	5.34e+40	5.13e+40	3.95e+40	8.27e-02
162712-24380	0.12	0.013	13.0	0.427	7.91e+41	5.64e+40	5.68e+40	5.63e+40	1.07e-01
162713-24295	0.29	0.017	15.6	0.408	1.84e+42	2.47e+41	1.61e+41	1.33e+41	1.47e-01
162715-24303	0.22	0.017	15.3	0.338	1.05e+42	1.48e+41	1.27e+41	1.17e+41	1.87e-01
162725-24273	0.70	0.023	13.4	0.425	4.61e+42	1.12e+42	3.03e+41	5.77e+41	2.16e-01
162727-24405	3.60	0.055	12.2	0.121	5.51e+42	1.20e+43	3.67e+42	4.24e+42	1.81e+00
162728-24271	0.97	0.022	13.3	0.384	5.43e+42	2.21e+42	2.74e+41	5.23e+41	2.77e-01
162728-24393	0.17	0.015	13.0	0.613	2.10e+42	1.02e+41	7.58e+40	7.73e+40	6.07e-02
162729-24274	0.57	0.023	13.0	0.282	2.01e+42	7.40e+41	2.83e+41	5.77e+41	3.97e-01
162730-24264	0.51	0.019	13.7	0.282	1.83e+42	7.06e+41	1.70e+41	3.41e+41	3.32e-01
162730-24415	0.61	0.029	13.0	0.313	2.49e+42	6.56e+41	5.58e+41	6.19e+41	3.68e-01
162733-24262	1.10	0.028	14.1	0.395	6.51e+42	2.25e+42	5.20e+41	1.06e+42	2.94e-01
162739-24424	0.37	0.023	11.8	0.133	5.87e+41	3.12e+41	2.61e+41	2.88e+41	7.34e-01
162740-24431	0.13	0.013	13.0	0.156	2.45e+41	6.62e+40	5.12e+40	5.64e+40	3.55e-01
162759-24334	0.63	0.025	11.0	0.134	9.55e+41	8.00e+41	3.57e+41	6.90e+41	9.68e-01
162821-24362	0.17	0.014	11.5	0.108	2.33e+41	1.07e+41	5.33e+40	1.10e+41	5.82e-01
163138-24495	1.10	0.031	12.2	0.173	2.18e+42	2.03e+42	3.79e+41	5.74e+41	6.85e-01
163139-24506	0.48	0.026	12.7	0.221	1.24e+42	4.52e+41	2.53e+41	3.62e+41	4.29e-01
163140-24485	0.24	0.018	9.9	0.215	5.45e+41	1.63e+41	8.09e+40	1.21e+41	3.35e-01

to be continued on the next page

Table 6.1: (continued from previous page)

Core Name[a]	Mass[a] ($M_\odot$)	$R_{\rm eff}$[a] (pc)	$T_{\rm k}$[b] (K)	$\sigma_{\rm obs}$[b] (km s^{-1})	$\Omega_{\rm k}$[c] (erg)	$-\Omega_{\rm g}$[c] (erg)	$-\Omega_{\rm P,w}$[c] (erg)	$-\Omega_{\rm P,t}$[c] (erg)	Virial[d] Ratio
163141-24495	0.89	0.029	12.2	0.182	1.84e+42	1.40e+42	3.79e+41	4.96e+41	6.16e-01
163154-24560	0.43	0.023	11.7	0.218	1.06e+42	4.08e+41	1.87e+41	2.54e+41	4.00e-01
163157-24572	0.78	0.031	11.1	0.136	1.20e+42	9.98e+41	3.87e+41	6.63e+41	8.53e-01
163201-24564	0.08	0.009	13.9	0.189	1.85e+41	3.76e+40	9.39e+39	1.44e+40	1.66e-01
163223-24284	7.60	0.041	13.8	0.231	2.15e+43	7.28e+43	1.44e+42	1.68e+42	1.76e+00
163229-24291	3.70	0.047	12.1	0.141	6.19e+42	1.51e+43	2.22e+42	2.50e+42	1.60e+00
163448-24381	0.66	0.031	8.8	0.152	9.74e+41	7.32e+41	3.45e+41	3.06e+41	7.10e-01
Chamaeleon I									
Cha1-C1	3.36	0.035	10.0	0.490	2.71e+43	1.64e+43	4.37e+41	1.33e+42	3.35e-01
Cha1-C2	1.62	0.046	10.0	0.480	1.26e+43	2.95e+42	8.79e+41	2.86e+42	2.66e-01
Cha1-C3	1.16	0.040	10.0	0.530	1.08e+43	1.72e+42	6.82e+41	1.94e+42	2.02e-01
Cha1-C4	0.66	0.035	10.0	0.230	1.63e+42	6.35e+41	4.51e+41	1.55e+42	8.08e-01
Cha1-C8	0.15	0.019	10.0	0.580	1.64e+42	5.99e+40	7.57e+40	2.16e+41	1.07e-01
Cha1-C9	0.68	0.044	10.0	0.320	2.68e+42	5.35e+41	4.47e+41	2.28e+42	6.07e-01
Cha1-C10	0.31	0.032	10.0	0.390	1.68e+42	1.53e+41	3.17e+41	1.01e+42	4.40e-01
Cha1-C11	0.76	0.052	10.0	0.290	2.59e+42	5.73e+41	1.34e+42	4.69e+42	1.28e+00
Cha1-C14	0.21	0.028	10.0	0.520	1.88e+42	8.15e+40	2.37e+41	6.45e+41	2.56e-01
Cha1-C19	0.28	0.036	10.0	0.310	1.05e+42	1.11e+41	5.64e+41	1.49e+42	1.03e+00
Cha1-C21	0.10	0.022	10.0	0.250	2.76e+41	2.30e+40	1.19e+41	3.46e+41	8.84e-01
Cha1-C29	0.17	0.029	10.0	0.570	1.80e+42	5.18e+40	2.15e+41	7.08e+41	2.71e-01
Cha1-C30	0.46	0.050	10.0	0.230	1.14e+42	2.18e+41	9.21e+41	4.19e+42	2.34e+00
Cha1-C31	0.28	0.038	10.0	0.190	5.52e+41	1.05e+41	4.87e+41	1.91e+42	2.27e+00
Cha1-C33	0.18	0.031	10.0	0.310	6.77e+41	5.35e+40	3.02e+41	1.02e+42	1.01e+00

to be continued on the next page

Table 6.1: (continued from previous page)

Core Name[a]	Mass[a] ($M_\odot$)	R_{eff}[a] (pc)	T_{k}[b] (K)	σ_{obs}[b] (km s^{-1})	Ω_{k}[c] (erg)	$-\Omega_{\mathrm{g}}$[c] (erg)	$-\Omega_{\mathrm{P,w}}$[c] (erg)	$-\Omega_{\mathrm{P,t}}$[c] (erg)	Virial[d] Ratio
Cha1-C34	0.50	0.052	10.0	0.300	1.79e+42	2.45e+41	8.44e+41	3.30e+42	1.23e+00
Cha1-C35	0.12	0.026	10.0	0.340	5.21e+41	2.83e+40	2.93e+41	7.07e+41	9.87e-01
Cha1-C40	0.23	0.035	10.0	0.190	4.53e+41	7.65e+40	5.30e+41	1.59e+42	2.42e+00
Cha1-C42	0.10	0.024	10.0	0.410	5.91e+41	2.12e+40	1.55e+41	4.25e+41	5.09e-01

[a] Starless dense core name, mass, and effective radius as adopted from Nutter & Ward-Thompson (2007); Jørgensen et al. (2008); Belloche et al. (2011) for all three regions respectively.

[b] Observed linewidth and kinetic temperature as measured from the GAS kinematic dataset. A stand-in value of $T = 10$ K is used for dense cores which have no temperature coverage (see Section 6.2 for details).

[c] Virial parameters as derived in Section 6.4.

[d] Indicates whether the dense core is bound taking into account all virial terms; $-(\Omega_{\mathrm{g}} + \Omega_{\mathrm{P,t}} + \Omega_{\mathrm{P,w}})/2\Omega_{\mathrm{k}}$.

Chapter 7

Conclusions

In this study, we present ALMA Cycle 3 Band 3 observations of 73 dense cores in the Orion B North region. We perform synthetic observations of starless core evolution simulations to predict the expected number of starless core detections in our dataset under the turbulent fragmentation model. We summarize our main results as follows:

1. We detect 34 continuum sources across 19 individual ALMA pointings. Four of these detections are most likely starless, as we find no protostellar association nor signs of CO outflow at their location.

2. The likely starless cores detected through our ALMA observations are among the faintest objects in our survey and all are associated with mid- to high-concentration parent cores, as measured by the lower-resolution NWT07 SCUBA data.

3. We generate synthetic observations of isolated starless core evolution simulations to predict the number of starless core detections expected under the turbulent fragmentation model. The number of starless core detections (1) agree with the predicted number of starless core detections (0.893) under the turbulent fragmentation model.

We put these results in the context of previous ALMA surveys by performing a multi-cloud virial analysis with dense core populations observed with ALMA. The Ophiuchus and Orion B North results are consistent with the turbulent fragmentation picture, while Chamaeleon I results are not. We perform an additional virial analysis on all three starless core populations, and find that Chamaeleon I shows features unlike both Ophiuchus and Orion B North. According to our simple Jeans analysis, the Chamaeleon I cores appear less bound. With the contributions of external pressure terms in our virial analysis, we show that an order of magnitude more of the binding energy is attributed to cloud weight and cloud-scale turbulent pressure than self-gravity, compared with the other two clouds. These differences lend weight to the findings of Tsitali et al. (2015), that the dense cores in Chamaeleon I, unlike the majority of cores in most star-forming regions, are destined to re-expand without forming stars.

7.1 Datasets, Funding, and Platform Acknowledgements

The National Radio Astronomy Observatory is a facility of the National Science Foundation operated under cooperative agreement by Associated Universities, Inc. This study makes use of the following ALMA data, with project codes: #2012.1.00031.S, #2013.1.00187.S, and #2015.1.00094.S. ALMA is a partnership of ESO (representing its member states), NSF (USA), and NINS (Japan), together with NRC (Canada) and NSC and ASIAA (Taiwan), in cooperation with the Republic of Chile. The Joint ALMA Observatory is operated by ESO, AUI/NRAO, and NAOJ. The JCMT has historically been operated by the Joint Astronomy Center on behalf of the Science and Technology Facilities Council of the United Kingdom, the National Research Council of Canada and the Netherlands Organisation for Scientific Research. The Green Bank Observatory is a facility of the National Science Foundation operated under cooperative agreement by Associated Universities, Inc. This research also made use of NASA's Astrophysics Data System (ADS) Abstract Service. This research has made use of the SIMBAD database, operated at CDS, Strasbourg, France (Wenger et al., 2000). The authors acknowledge the use of the Canadian Advanced Network for Astronomy Research (CANFAR) Science Platform. Our work used the facilities of the Canadian Astronomy Data Center, operated by the National Research Council of Canada with the support of the Canadian Space Agency, and CANFAR, a consortium that serves the data-intensive storage, access, and processing needs of university groups and centers engaged in astronomy research (Gaudet et al., 2010). We thank the GAS Team for their publicly available DR1 dataset. Samuel Fielder and Helen Kirk acknowledge support from an NSERC Discovery Grant, as it pertains to the work completed for this thesis work.

Facilities: ALMA, JCMT (SCUBA-1, SCUBA-2), GBT (KFPA)

Software: (CASA, The CASA Team et al., 2022), (Astropy, Astropy Collaboration et al., 2013, 2018, 2022), (Matplotlib, Hunter, 2007)

Bibliography

Astropy Collaboration, Robitaille, T. P., Tollerud, E. J., et al. 2013, Astronomy and Astrophysics, 558, A33, doi: 10.1051/0004-6361/201322068

Astropy Collaboration, Price-Whelan, A. M., Sipőcz, B. M., et al. 2018, The Astronomical Journal, 156, 123, doi: 10.3847/1538-3881/aabc4f

Astropy Collaboration, Price-Whelan, A. M., Lim, P. L., et al. 2022, The Astrophysical Journal, 935, 167, doi: 10.3847/1538-4357/ac7c74

Ballesteros-Paredes, J., Klessen, R. S., Mac Low, M. M., & Vazquez-Semadeni, E. 2007, Molecular Cloud Turbulence and Star Formation (eprint: arXiv:astro-ph/0603357), 63, doi: 10.48550/arXiv.astro-ph/0603357

Belloche, A., Parise, B., van der Tak, F. F. S., et al. 2006, Astronomy and Astrophysics, 454, L51, doi: 10.1051/0004-6361:20065306

Belloche, A., Schuller, F., Parise, B., et al. 2011, Astronomy and Astrophysics, 527, A145, doi: 10.1051/0004-6361/201015733

Bergin, E. A., & Tafalla, M. 2007, Annual Review of Astronomy and Astrophysics, 45, 339, doi: 10.1146/annurev.astro.45.071206.100404

Bertoldi, F., & McKee, C. F. 1992, The Astrophysical Journal, 395, 140, doi: 10.1086/171638

Bohlin, R. C., Savage, B. D., & Drake, J. F. 1978, The Astrophysical Journal, 224, 132, doi: 10.1086/156357

Bonnor, W. B. 1956, Monthly Notices of the Royal Astronomical Society, 116, 351, doi: 10.1093/mnras/116.3.351

Boulanger, F., Bronfman, L., Dame, T. M., & Thaddeus, P. 1998, Astronomy and Astrophysics, 332, 273

Caselli, P., Pineda, J. E., Zhao, B., et al. 2019, The Astrophysical Journal, 874, 89, doi: 10.3847/1538-4357/ab0700

Chen, M. C.-Y., Di Francesco, J., Johnstone, D., et al. 2016, The Astrophysical Journal, 826, 95, doi: 10.3847/0004-637X/826/1/95

Chen, X., Arce, H. G., Zhang, Q., et al. 2013, The Astrophysical Journal, 768, 110, doi: 10.1088/0004-637X/768/2/110

Dame, T. M., Hartmann, D., & Thaddeus, P. 2001, The Astrophysical Journal, 547, 792, doi: 10.1086/318388

Dame, T. M., & Thaddeus, P. 2022, The Astrophysical Journal Supplement Series, 262, 5, doi: 10.3847/1538-4365/ac7e53

de Geus, E. J., Bronfman, L., & Thaddeus, P. 1990, Astronomy and Astrophysics, 231, 137

di Francesco, J., Evans, II, N. J., Caselli, P., et al. 2007, An Observational Perspective of Low-Mass Dense Cores I: Internal Physical and Chemical Properties (eprint: arXiv:astro-ph/0602379), 17, doi: 10.48550/arXiv.astro-ph/0602379

Dunham, M. M., Allen, L. E., Evans, II, N. J., et al. 2015, The Astrophysical Journal Supplement Series, 220, 11, doi: 10.1088/0067-0049/220/1/11

Dunham, M. M., Offner, S. S. R., Pineda, J. E., et al. 2016, The Astrophysical Journal, 823, 160, doi: 10.3847/0004-637X/823/2/160

Dutta, S., Lee, C.-F., Liu, T., et al. 2020, The Astrophysical Journal Supplement Series, 251, 20, doi: 10.3847/1538-4365/abba26

Ebert, R. 1955, Zeitschrift fur Astrophysik, 37, 217

Enoch, M. L., Glenn, J., Evans, II, N. J., et al. 2007, The Astrophysical Journal, 666, 982, doi: 10.1086/520321

Fang, M., van Boekel, R., Wang, W., et al. 2009, Astronomy and Astrophysics, 504, 461, doi: 10.1051/0004-6361/200912468

Federman, S., Megeath, S. T., Tobin, J. J., et al. 2023, The Astrophysical Journal, 944, 49, doi: 10.3847/1538-4357/ac9f4b

Fischer, W. J., Megeath, S. T., Ali, B., et al. 2010, Astronomy and Astrophysics, 518, L122, doi: 10.1051/0004-6361/201014636

Flaherty, K. M., & Muzerolle, J. 2008, The Astronomical Journal, 135, 966, doi: 10.1088/0004-6256/135/3/966

Friesen, R. K., Pineda, J. E., co-PIs, et al. 2017, The Astrophysical Journal, 843, 63, doi: 10.3847/1538-4357/aa6d58

Furlan, E., Fischer, W. J., Ali, B., et al. 2016, The Astrophysical Journal Supplement Series, 224, 5, doi: 10.3847/0067-0049/224/1/5

Gaudet, S., Hill, N., Armstrong, P., et al. 2010, in SPIE Astronomical Telescopes + Instrumentation, ed. N. M. Radziwill & A. Bridger, San Diego, California, USA, 77401I, doi: 10.1117/12.858026

Girichidis, P., Konstandin, L., Whitworth, A. P., & Klessen, R. S. 2014, The Astrophysical Journal, 781, 91, doi: 10.1088/0004-637X/781/2/91

Goodwin, S. P., Nutter, D., Kroupa, P., Ward-Thompson, D., & Whitworth, A. P. 2008, Astronomy and Astrophysics, 477, 823, doi: 10.1051/0004-6361:20078452

Holman, K., Walch, S. K., Goodwin, S. P., & Whitworth, A. P. 2013, Monthly Notices of the Royal Astronomical Society, 432, 3534, doi: 10.1093/mnras/stt705

Hunter, J. D. 2007, Computing in Science & Engineering, 9, 90, doi: 10.1109/MCSE.2007.55

Jessop, N. E., & Ward-Thompson, D. 2000, Monthly Notices of the Royal Astronomical Society, 311, 63, doi: 10.1046/j.1365-8711.2000.03011.x

Jijina, J., Myers, P. C., & Adams, F. C. 1999, The Astrophysical Journal Supplement Series, 125, 161, doi: 10.1086/313268

Johnstone, D., Rosolowsky, E., Tafalla, M., & Kirk, H. 2010, The Astrophysical Journal, 711, 655, doi: 10.1088/0004-637X/711/2/655

Johnstone, D., Wilson, C. D., Moriarty-Schieven, G., et al. 2000, The Astrophysical Journal, 545, 327, doi: 10.1086/317790

Jørgensen, J. K., Johnstone, D., Kirk, H., & Myers, P. C. 2007, The Astrophysical Journal, 656, 293, doi: 10.1086/510150

Jørgensen, J. K., Johnstone, D., Kirk, H., et al. 2008, The Astrophysical Journal, 683, 822, doi: 10.1086/589956

Juvela, M., Demyk, K., Doi, Y., et al. 2015, Astronomy and Astrophysics, 584, A94, doi: 10.1051/0004-6361/201425269

Kauffmann, J., Bertoldi, F., Bourke, T. L., Evans, II, N. J., & Lee, C. W. 2008, Astronomy and Astrophysics, 487, 993, doi: 10.1051/0004-6361:200809481

Keown, J., Di Francesco, J., Kirk, H., et al. 2017, The Astrophysical Journal, 850, 3, doi: 10.3847/1538-4357/aa93ec

Kerr, R., Kirk, H., Di Francesco, J., et al. 2019, The Astrophysical Journal, 874, 147, doi: 10.3847/1538-4357/ab0c08

Kirk, H., Johnstone, D., & Di Francesco, J. 2006, The Astrophysical Journal, 646, 1009, doi: 10.1086/503193

Kirk, H., Francesco, J. D., Johnstone, D., et al. 2016, The Astrophysical Journal, 817, 167, doi: 10.3847/0004-637X/817/2/167

Kirk, H., Dunham, M. M., Di Francesco, J., et al. 2017a, The Astrophysical Journal, 838, 114, doi: 10.3847/1538-4357/aa63f8

Kirk, H., Friesen, R. K., Pineda, J. E., et al. 2017b, The Astrophysical Journal, 846, 144, doi: 10.3847/1538-4357/aa8631

Könyves, V., André, Ph., Men'shchikov, A., et al. 2015, Astronomy and Astrophysics, 584, A91, doi: 10.1051/0004-6361/201525861

Könyves, V., André, Ph., Arzoumanian, D., et al. 2020, Astronomy & Astrophysics, 635, A34, doi: 10.1051/0004-6361/201834753

Kramer, C., Stutzki, J., Rohrig, R., & Corneliussen, U. 1998, Astronomy and Astrophysics, 329, 249

Kuruwita, R. L., & Haugbølle, T. 2023, Astronomy and Astrophysics, 674, A196, doi: 10.1051/0004-6361/202244882

Li, P., Cunningham, A., Gaches, B., et al. 2021, The Journal of Open Source Software, 6, 3771, doi: 10.21105/joss.03771

Lomax, O., Whitworth, A. P., Hubber, D. A., Stamatellos, D., & Walch, S. 2015, Monthly Notices of the Royal Astronomical Society, 447, 1550, doi: 10.1093/mnras/stu2530

Mac Low, M.-M., & Klessen, R. S. 2004, Reviews of Modern Physics, 76, 125, doi: 10.1103/RevModPhys.76.125

Marton, G., Tóth, L. V., Paladini, R., et al. 2016, Monthly Notices of the Royal Astronomical Society, 458, 3479, doi: 10.1093/mnras/stw398

McKee, C. F. 1989, The Astrophysical Journal, 345, 782, doi: 10.1086/167950

Megeath, S. T., Gutermuth, R., Muzerolle, J., et al. 2012, The Astronomical Journal, 144, 192, doi: 10.1088/0004-6256/144/6/192

Moe, M., & Di Stefano, R. 2017, The Astrophysical Journal Supplement Series, 230, 15, doi: 10.3847/1538-4365/aa6fb6

Motte, F., Andre, P., & Neri, R. 1998, Astronomy and Astrophysics, 336, 150

Motte, F., Bontemps, S., Schilke, P., et al. 2007, Astronomy and Astrophysics, 476, 1243, doi: 10.1051/0004-6361:20077843

Murillo, N. M., Van Dishoeck, E. F., Hacar, A., Harsono, D., & Jørgensen, J. K. 2022, Astronomy & Astrophysics, 658, A53, doi: 10.1051/0004-6361/202141250

Nutter, D., & Ward-Thompson, D. 2007, Monthly Notices of the Royal Astronomical Society, 374, 1413, doi: 10.1111/j.1365-2966.2006.11246.x

Offner, S. S. R., Capodilupo, J., Schnee, S., & Goodman, A. A. 2012, Monthly Notices of the Royal Astronomical Society: Letters, 420, L53, doi: 10.1111/j.1745-3933.2011.01194.x

Offner, S. S. R., Clark, P. C., Hennebelle, P., et al. 2014, The Origin and Universality of the Stellar Initial Mass Function (eprint: arXiv:1312.5326), 53–75, doi: 10.2458/azu_uapress_9780816531240-ch003

Offner, S. S. R., Taylor, J., Markey, C., et al. 2022, Monthly Notices of the Royal Astronomical Society, 517, 885, doi: 10.1093/mnras/stac2734

Ossenkopf, V., & Henning, Th. 1994, Astronomy and Astrophysics, 291, 943

Pattle, K., Ward-Thompson, D., Kirk, J. M., et al. 2015, Monthly Notices of the Royal Astronomical Society, 450, 1094, doi: 10.1093/mnras/stv376

Pineda, J. E., Rosolowsky, E. W., & Goodman, A. A. 2009, The Astrophysical Journal, 699, L134, doi: 10.1088/0004-637X/699/2/L134

Pineda, J. E., Segura-Cox, D., Caselli, P., et al. 2020, Nature Astronomy, 4, 1158, doi: 10.1038/s41550-020-1150-z

Pineda, J. E., Arzoumanian, D., Andre, P., et al. 2023, 534, 233, doi: 10.48550/arXiv.2205.03935

Rowles, J., & Froebrich, D. 2009, Monthly Notices of the Royal Astronomical Society, 395, 1640, doi: 10.1111/j.1365-2966.2009.14655.x

Sadavoy, S. I., Di Francesco, J., Johnstone, D., et al. 2013, The Astrophysical Journal, 767, 126, doi: 10.1088/0004-637X/767/2/126

Sahu, D., Liu, S.-Y., Liu, T., et al. 2021, The Astrophysical Journal, 907, L15, doi: 10.3847/2041-8213/abd3aa

Schnee, S., Enoch, M., Johnstone, D., et al. 2010, The Astrophysical Journal, 718, 306, doi: 10.1088/0004-637X/718/1/306

Shirley, Y. L., Huard, T. L., Pontoppidan, K. M., et al. 2011, The Astrophysical Journal, 728, 143, doi: 10.1088/0004-637X/728/2/143

Spezzi, L., Petr-Gotzens, M. G., Alcalá, J. M., et al. 2015, Astronomy & Astrophysics, 581, A140, doi: 10.1051/0004-6361/201425417

Stutz, A. M., Tobin, J. J., Stanke, T., et al. 2013, The Astrophysical Journal, 767, 36, doi: 10.1088/0004-637X/767/1/36

Stutzki, J., & Guesten, R. 1990, The Astrophysical Journal, 356, 513, doi: 10.1086/168859

The CASA Team, Bean, B., Bhatnagar, S., et al. 2022, Publications of the Astronomical Society of the Pacific, 134, 114501, doi: 10.1088/1538-3873/ac9642

Tobin, J. J., Hartmann, L., Looney, L. W., & Chiang, H.-F. 2010, The Astrophysical Journal, 712, 1010, doi: 10.1088/0004-637X/712/2/1010

Tobin, J. J., Looney, L. W., Li, Z.-Y., et al. 2016, The Astrophysical Journal, 818, 73, doi: `10.3847/0004-637X/818/1/73`

Tobin, J. J., Sheehan, P. D., Megeath, S. T., et al. 2020, The Astrophysical Journal, 890, 130, doi: `10.3847/1538-4357/ab6f64`

Tokuda, K., Fujishiro, K., Tachihara, K., et al. 2020, The Astrophysical Journal, 899, 10, doi: `10.3847/1538-4357/ab9ca7`

Tsitali, A. E., Belloche, A., Commerçon, B., & Menten, K. M. 2013, Astronomy and Astrophysics, 557, A98, doi: `10.1051/0004-6361/201321204`

Tsitali, A. E., Belloche, A., Garrod, R. T., Parise, B., & Menten, K. M. 2015, Astronomy and Astrophysics, 575, A27, doi: `10.1051/0004-6361/201322955`

Ward-Thompson, D., Scott, P. F., Hills, R. E., & Andre, P. 1994, Monthly Notices of the Royal Astronomical Society, 268, 276, doi: `10.1093/mnras/268.1.276`

Ward-Thompson, D., Di Francesco, J., Hatchell, J., et al. 2007, Publications of the Astronomical Society of the Pacific, 119, 855, doi: `10.1086/521277`

Wenger, M., Ochsenbein, F., Egret, D., et al. 2000, Astronomy and Astrophysics Supplement Series, 143, 9, doi: `10.1051/aas:2000332`

Williams, J. P., de Geus, E. J., & Blitz, L. 1994, The Astrophysical Journal, 428, 693, doi: `10.1086/174279`

Wilson, B. A., Dame, T. M., Masheder, M. R. W., & Thaddeus, P. 2005, Astronomy and Astrophysics, 430, 523, doi: `10.1051/0004-6361:20035943`

Zamora-Avilés, M., & Vázquez-Semadeni, E. 2014, The Astrophysical Journal, 793, 84, doi: `10.1088/0004-637X/793/2/84`

Zucker, C., Speagle, J. S., Schlafly, E. F., et al. 2019, The Astrophysical Journal, 879, 125, doi: `10.3847/1538-4357/ab2388`

Appendix A

Additional Information

A.1 Comparison of SCUBA and SCUBA-2 data

While not available at the time of the ALMA proposal, the Orion molecular cloud was observed by the JCMT Gould Belt Survey with the SCUBA-2 instrument (Kirk et al., 2016), which has larger spatial coverage and improved sensitivity compared to the NWT07 SCUBA(-1) observations. The SCUBA(-1) NWT07 measurements has a sensitivity of 16 mJy beam^{-1} at 850μm, while comparatively, the SCUBA-2 observations by Kirk et al. (2016) has a sensitivity of 3.4 mJy beam^{-1} at the same wavelength. Additionally, two differing core finding algorithms were used to identify over dense structures in the emission maps, leading to slightly different core positions and footprints when looking at the same star forming region. For example, in Figure 3.4, the two ALMA observations for this paper (derived from the NWT07 catalog) lie approximately in between 3 distinct SCUBA-2 cores, as shown by the light blue contours over-plotted. While we use the SCUBA(-1) observations for most of our analysis, the SCUBA-2 cores are mentioned when important context is needed.

Each peak flux position from the SCUBA(-1) dataset was associated with the SCUBA-2 core whose boundary it lies within, resulting in all 100 SCUBA(-1) cores finding an association with a SCUBA-2 core (Kirk et al., 2016). Associated core values agree reasonably well between the two datasets, with some scatter present when looking at one-to-one relationships (Kirk et al., 2016). We do note that the relationship is not uniquely one-to-one, with respect to the associations, some SCUBA(-1) cores map to similar SCUBA-2 cores.

A.2 Additional Figures

Present in this section, are all leftover continuum images of our ALMA detections not shown in the main text. All detections present in these following images are directly associated with a protostellar source. Details are found in Section 3.2.

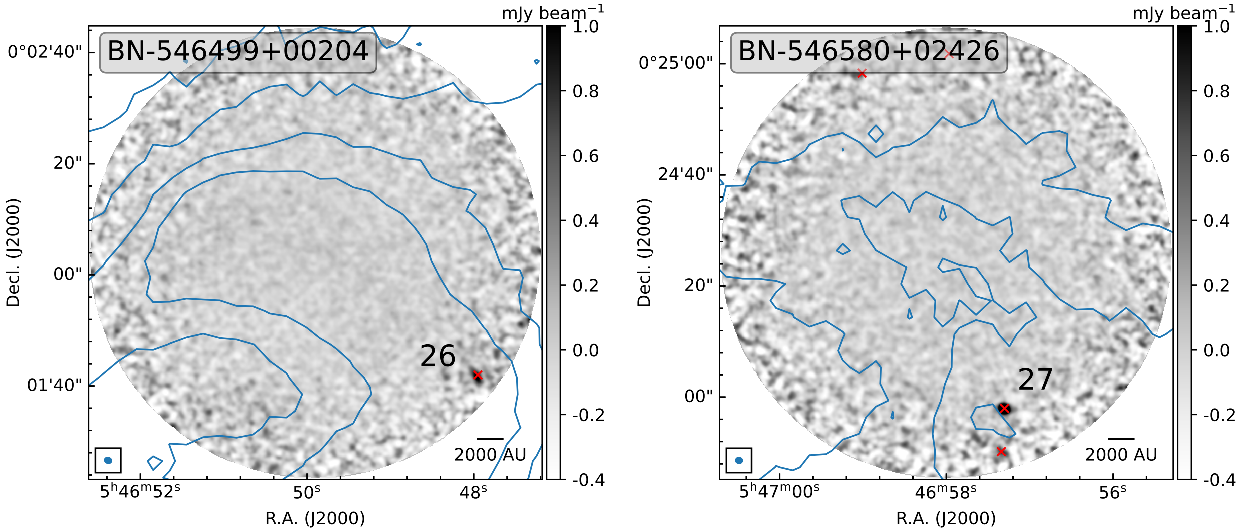

(a) BN-546499+00204

(b) BN-546580+02426

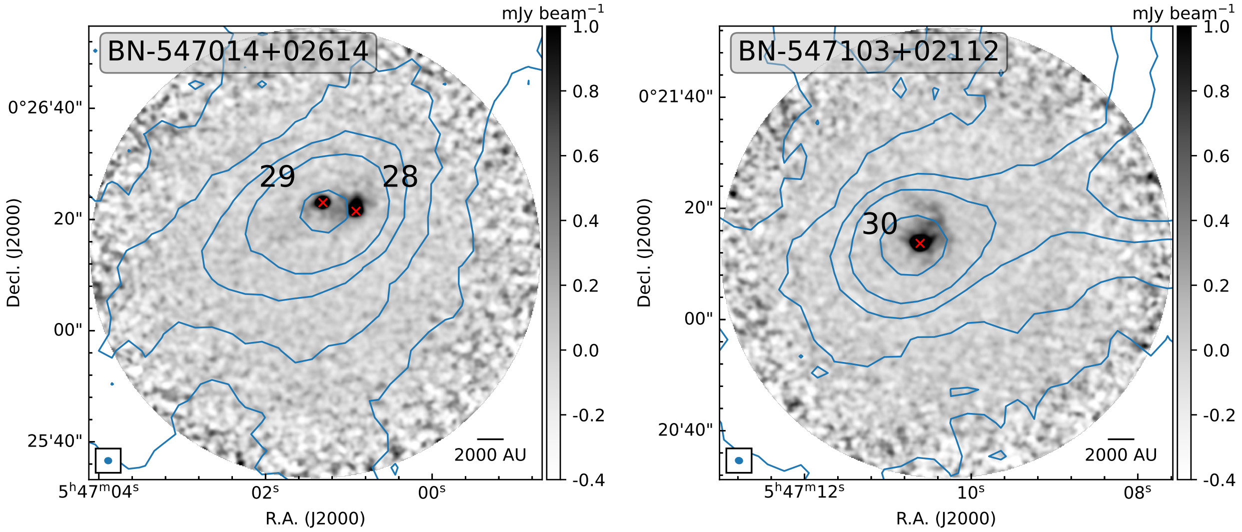

(c) BN-547014+02614

(d) BN-547103+02112

Figure A.1: ALMA single pointing fields that harbor detections. See Figure 3.2 for plotting conventions. All detections in these mosaic pointings have an associated protostellar association.

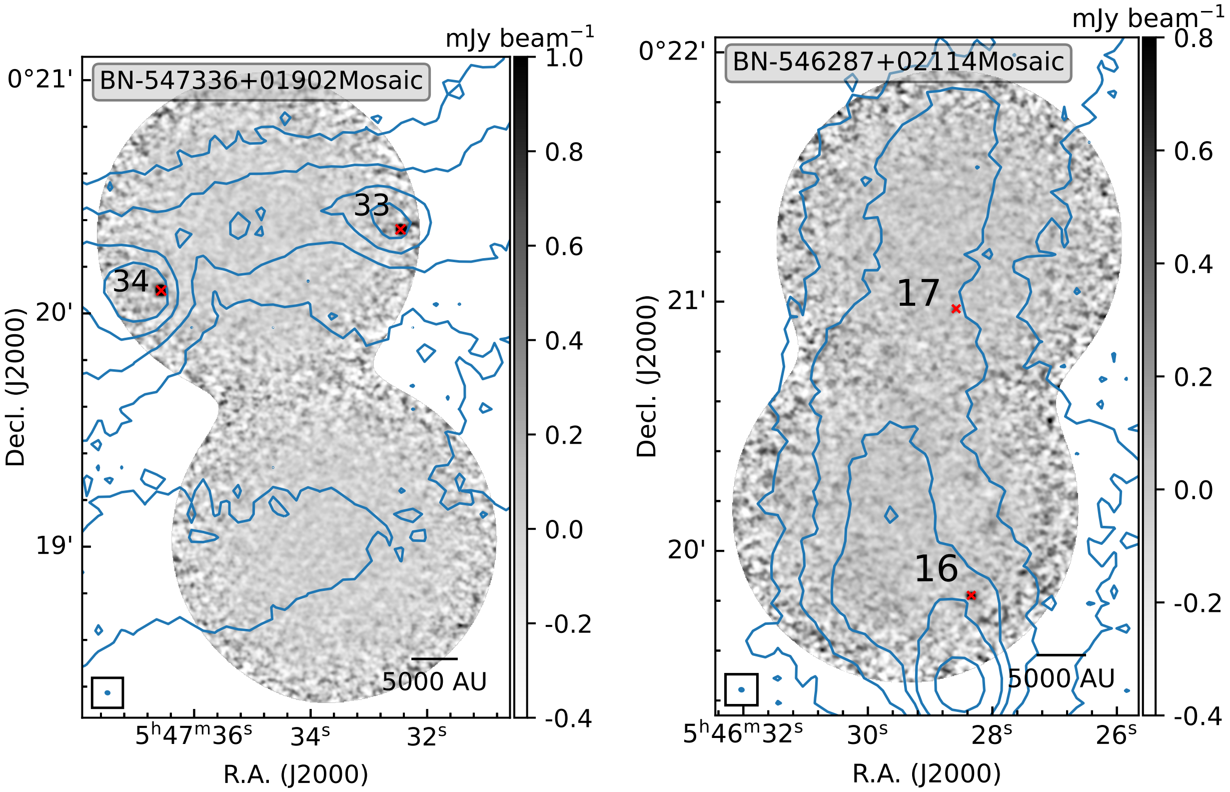

(a) BN-547336+01902Mosaic

(b) BN-546287+02114Mosaic

Figure A.2: ALMA mosaic fields that harbor detections. See Figure 3.2 for plotting conventions. All detections in these mosaic pointings have an associated protostellar association.

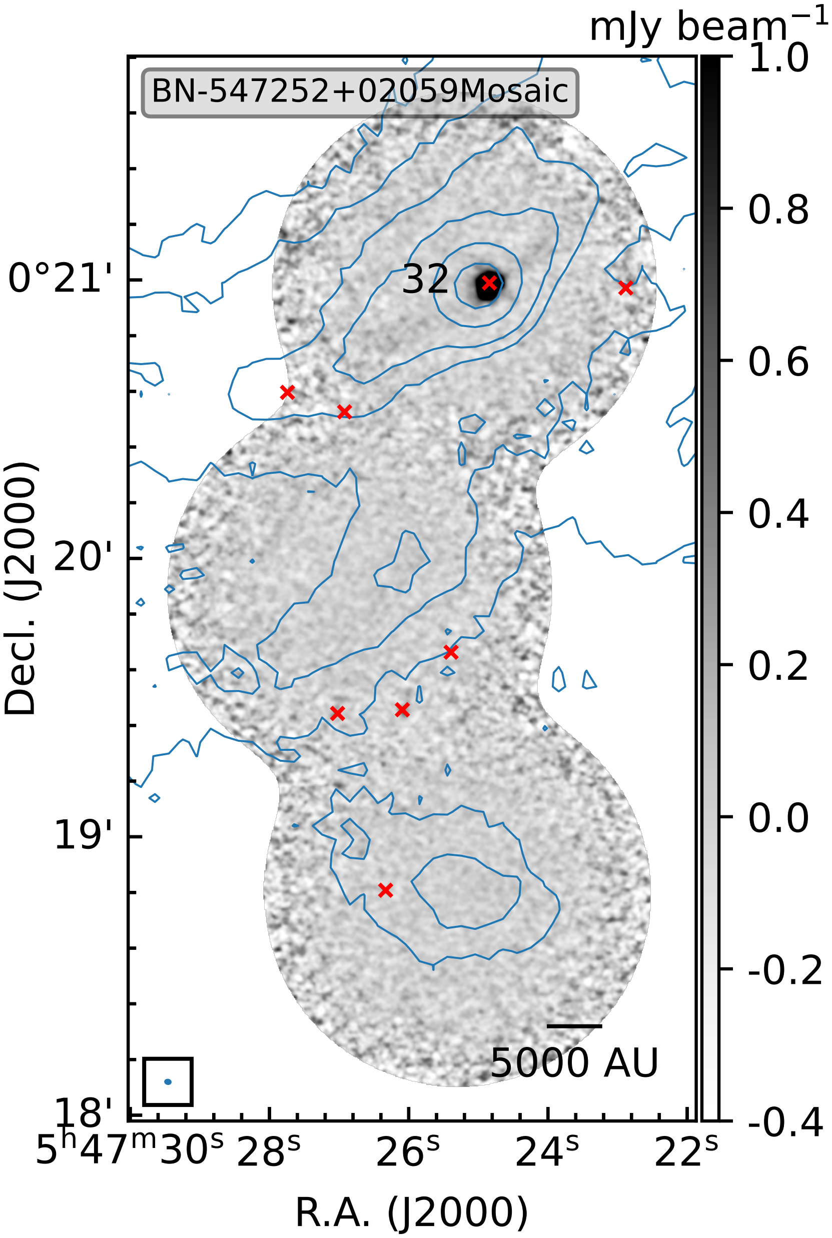

Figure A.3: ALMA mosaic field that harbor detections. See Figure 3.2 for plotting conventions. All detections in these mosaic pointings have an associated protostellar association.

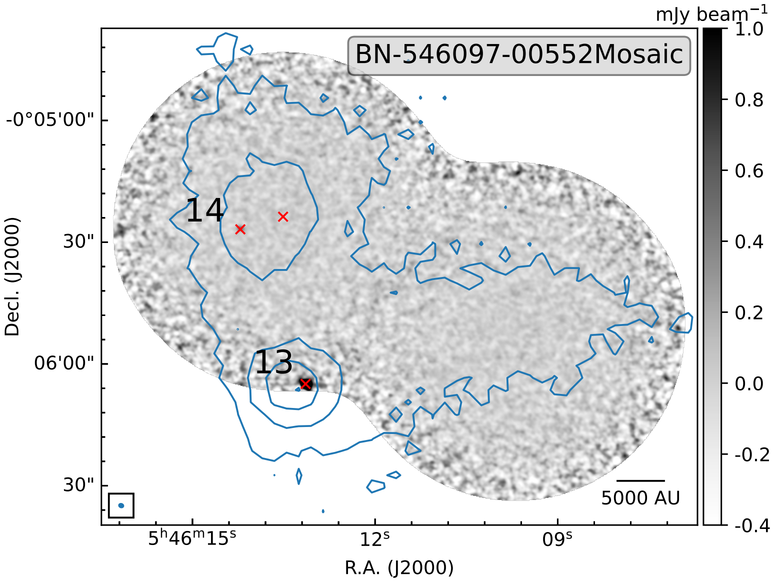

(a) BN-546097-00552Mosaic

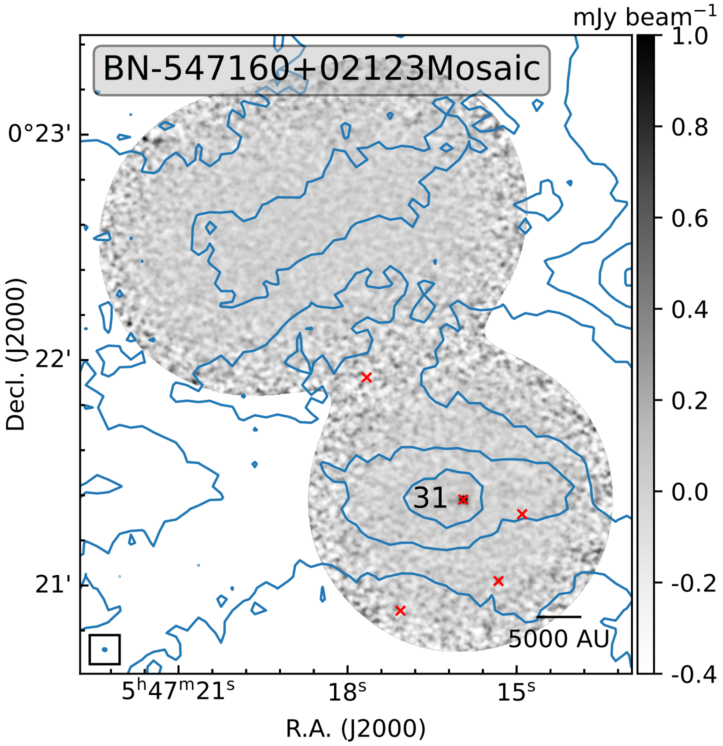

(b) BN-547160+02123Mosaic

Figure A.4: ALMA mosaic fields that harbor detections. See Figure 3.2 for plotting conventions. All detections in these mosaic pointings have an associated protostellar association.

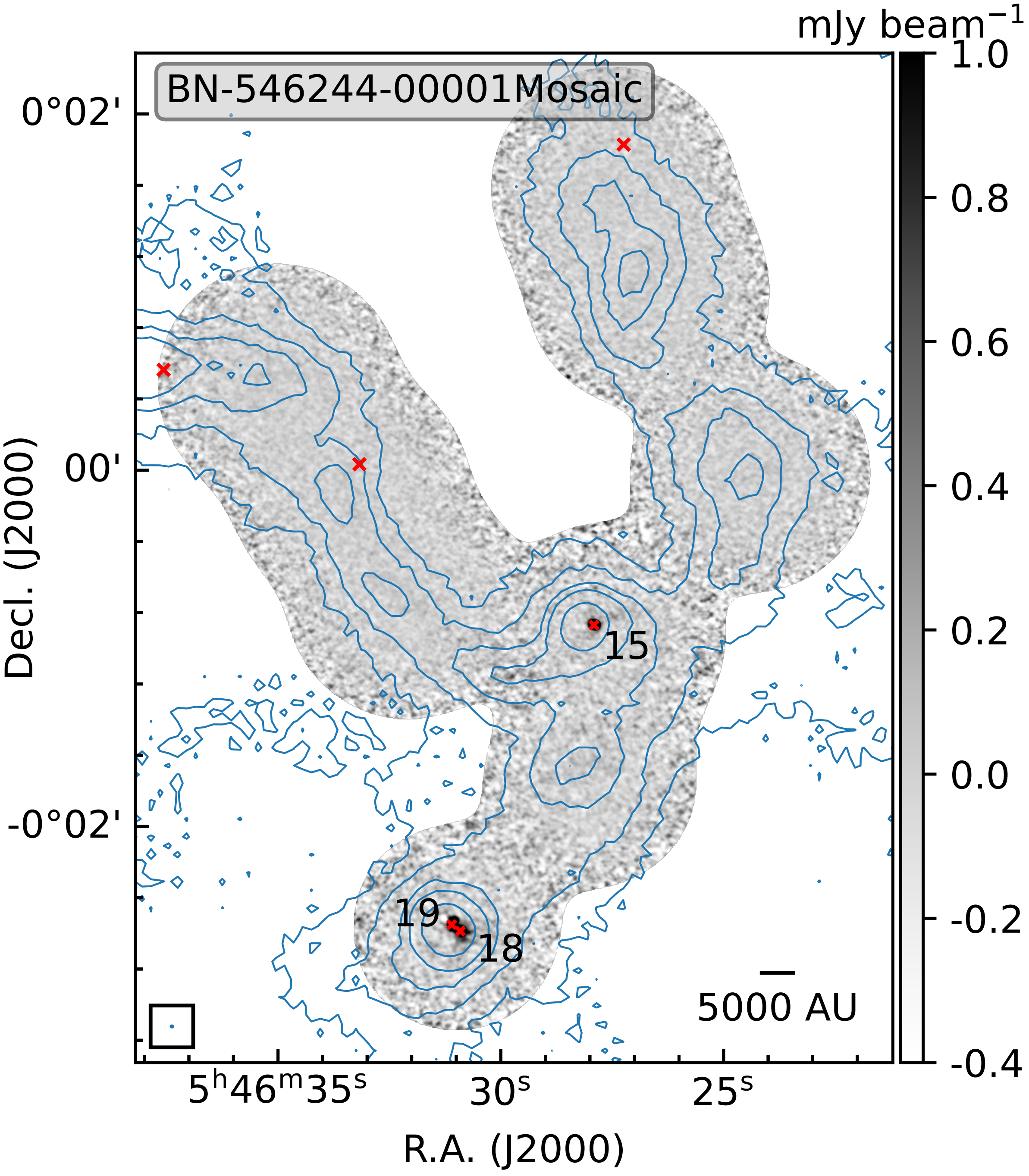

Figure A.5: ALMA mosaic field BN-546244-00001 that harbor detections. See Figure 3.2 for plotting conventions. All detections in these mosaic pointings have an associated protostellar association.